POLITECNICO DI TORINO

Master's Degree in Aerospace Engineering

Politecnico di Torino

Master's Degree Thesis

Analysis of impact of a radar antenna mispointing for the WIVERN doppler wind radar ESA earth explorer mission

Supervisors

Prof. Alessandro BATTAGLIA

Prof. Fabrizio STESINA

Candidate

Agostino NICOLÒ COZZUPOLI

April 2024

Science can amuse and fascinate us all,
but it is engineering that changes the world.
Isaac Asimov

La scienza può divertire e affascinare tutti noi,
ma è l'ingegneria a cambiare il mondo.
Isaac Asimov

Summary

Earth observation satellites are an increasingly important tool for studying the behavior of the Earth's atmosphere and even more for the behavior of climatological phenomena. In these cases, the critical point of modern science and engineering is effectivily the monitoring and development of increasingly accurate predictive models.
WIVERN (Wind Velocity Radar Nephoscope) mission aims to measure atmospheric winds with innovative precision in the field. This is done employing a Doppler radar, characterized by a section of the electromagnetic spectrum in the W band, which is a region with a wavelength of approximately 4 – 2.7 mm and covers the respective range between 110 GHz and 75 GHz. It is also necessary to calculate the reflectivity of the Earth's surface to obtain these measurements. This helps to decouple from the taken measurements every contribution that is not related to hydrometeors.
This work proposes a MATLAB-simulator to precisely calculate this quantity, integrating the reflected power of the radar signal from the surface. The western part of Piedmont has been chosen as a region of interest to test the simulator with an accurate and very particular orographic profile.
All the georeferenced information, including the elevation value, is included in a matrix of points known as the Digital Elevation Model (DEM), obtained from the website EarthData (supplied by NASA). These data are the starting point for calculating the power equation and transmission power, wavelength, and other constants.
The software model computes and processes variables such as the point-satellite distance, the projection of the antenna gain on the surface, the backscattering cross-section of the radar, and the area of the projected surface for each pixel. However, since each pixel is characterized by different georeferenced information, a vectorization process has been developed and used to obtain all the values required for analysis. Moreover, part of the model calculates which points are in the shadow of the satellite so as not to calculate their contribution to the final integral.
Once the integral has been calculated, the corresponding reflectivity value is obtained through an equation that links the different quantities. Many of the variables

evaluated and examined during the program are then schematized in tables and figures to describe better how the tool works.

Keywords*: WIVERN, Doppler radar, Digital, Elevation Model (DEM), Reflectivity, MATLAB simulator, Atmospheric wind measurement.*

Table of Contents

List of Figures

Acronyms

ESA
: European Space Agency

LDR
: Linear Depolarization Ratio

NASA
: National Aeronautics and Space Administration

RCS
: Radar Cross Section

WIVERN
: Wind Velocity Radar Nephoscope

Chapter 1

Introduction

Dedicated Earth observation satellites play a crucial role in addressing and understanding environmental and climate phenomena. These satellites provide a unique and global perspective on the Earth, enabling the monitoring and study of climate change, meteorology, land cover, air pollution, and many other environmental aspects. These data are essential for the sustainable management of our planet. Climate change in particular is one of the most pressing problems facing humanity today. The effects of global warming, such as rising sea levels, extreme weather events and loss of biodiversity, are having a significant impact on communities and ecosystems around the world. Earth observation satellites play a key role in monitoring the signs of these changes, providing data on temperature, sea level, greenhouse gas concentration, and other key parameters. These satellites make it possible to collect long-term data on a global scale, creating time series that are essential for analyzing trends and changes over time. They also provide real-time information that can be used to predict extreme weather events, monitor the spread of forest fires, study the dynamics of air masses, and much more.

The **WIVERN**, short for WInd VElocity Radar Nephoscope (`www.wivern.polito.it`, [1, 2, 3, 4, 5]), currently in Phase A, is one of the two remaining candidate missions with the final selection scheduled for July 2025.
The mission aims to measure atmospheric winds on a global scale and is expected to be critically important for improving weather forecasting and reducing the risk of high-impact weather events [6].

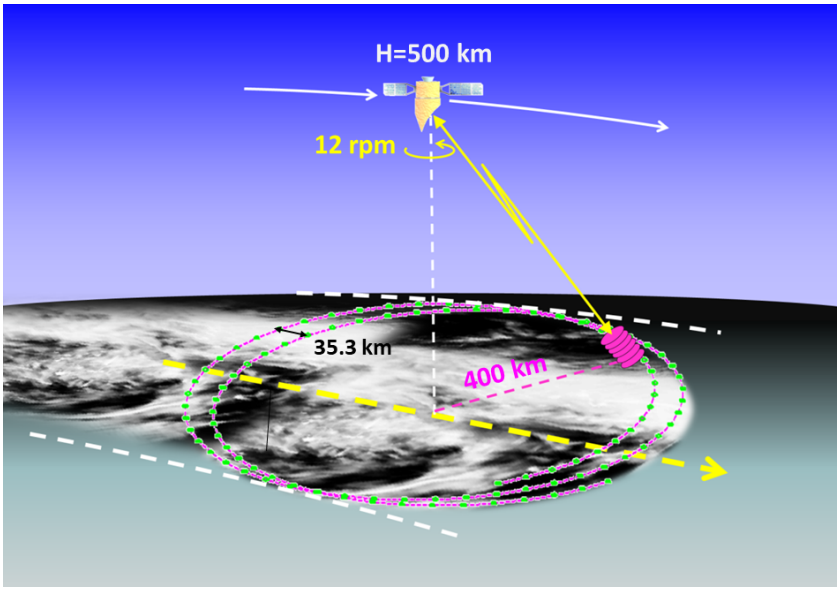

Figure 1.1: Artistic impression of the WIVERN mission. The 94 GHz Doppler radar performs a conical scan with an angle of incidence of 42° at 12 rpm which traces a cycloid on the ground (figure extracted from [7]).

Key points of the WIVERN mission include:

- **Measuring winds**: The WIVERN satellite would be equipped with a 94 GHz radar, which would measure the wind speed component along the line of sight based on an innovative Doppler technique that involves polarization diversity pulse pair processing [8, 9]. These measurements would provide detailed data on wind speed within clouds and precipitation systems [1]. A schematic of the system is shown in Figure 1.1.

- **Improving weather forecasting**, which is the main goal of the mission being so crucial in preventing and mitigating the impacts of weather disasters, such as hurricanes [6], storms, floods, and other extreme weather conditions. Improving weather forecasting means having a more accurate understanding of the initial conditions of the atmosphere, which are critical to feeding numerical weather prediction (NWP) models. Data collected by the WIVERN satellite, which measures wind speeds within clouds and precipitation systems, will contribute significantly to improving these initial conditions. Weather prediction models rely on this information to provide short- and long-term forecasts. Thus, having more accurate atmospheric wind data will better anticipate extreme weather events and prepare communities to deal with them more effectively.

- **Observational requirements**, which are a key element for mission success. These requirements set the standards and specifications for the data that the satellite must collect to meet the needs of the meteorological and scientific community. They include a very detailed vertical resolution, which is essential to better understand the structure of winds within clouds and precipitation systems; and a short observation cycle so that the satellite will make frequent measurements, which is particularly important for dynamic and rapidly changing weather events. Finally, global coverage, thanks to an altitude of 500 km of the satellite, would track widely over the Earth's surface, allowing repeated observations in different areas. This would allow coverage of many important regions, including the polar regions to ensure a global view of atmospheric winds.

In summary, the WIVERN mission represents a leap forward in Earth observation and understanding of its weather and climate processes, with a potentially revolutionary impact on weather prediction and our knowledge of our planet as it will be the first space mission to provide measurements of wind speed inside clouds, helping to close the existing gap in the WMO Global Observing System. This will contribute substantially to numerical weather prediction (NWP) and climatological research by providing unprecedented data on atmospheric dynamics.

In addition, the WIVERN satellite will produce high-resolution profiles of precipitation reflectivity, including rain, snow, and ice. These data will be invaluable for better quantification of the Earth's hydrologic cycle and energy budgets on our planet. With significantly reduced sampling errors compared to current and future radar cloud missions, we will be able to gain a more precise and detailed understanding of how water and energy move through our atmosphere and on Earth [10]. The role of this work in support of the mission will be to develop a simulator to reproduce the power and Doppler response of a real surface hit by the signal emitted by the antenna, also called "clutter".

1.1 Goals of the work

To obtain accurate wind speed measurements, it is essential to know very precisely the direction in which the radar antenna is pointed. By incorporating a realistic power spectral density derived from initial industrial studies, the error due to mis-pointing is expected to remains below 0.2 $\mathrm{m\,s^{-1}}$, especially if Doppler calibration is performed [2, 11]; therefore, it will make a very limited contribution to the Doppler velocity error budget.

In the next section, we will analyze the main objectives of the thesis related to the WIVERN mission, identifying the main challenges faced during the study process and aiming to provide a clear understanding of the intentions and scope of the research work.
They can be summarised in three main points.

Characterisation of the signal to clutter ratio

The first fundamental point for the WIVERN mission is to be able to characterize the signal to clutter ratio at any given height for an atmospheric target with a given reflectivity. The power return signal received from the ground, also known as clutter, is an obstacle that spoils the data received from the atmosphere (which is the actual target of the WIVERN mission), thus creating a 'blind zone' in the proximity of the surface. This is particularly relevant for detecting and quantifying the precipitation (rain or snow) near the surface [12, 13].
The vertical extent of this blind zone is largely determined by the surface type and is smaller over the ocean and larger over land or sea ice [14]. A study of this obstacle zone shows that for CloudSat, it has been shown that over land, the received signal is free from ground clutter only from the fifth range bin above ground level 1200 meter. New spaceborne radars such as the dual-frequency radar on board the Global Precipitation Measurement (GPM) Core Observatory or the Cloud Profiling Radar (CPR) on board the Earth Clouds, Aerosols, and Radiation Explorer (EarthCARE) mission expected to achieve smaller blind zones ranging between 600 meter and 1000 meter above surface (depending on radar operation mode).
These observational blind zones are likely to introduce errors in the derived statistics of snowfall frequency for surface level if the snowfall properties are significantly altered within the blind zone. For example, the snowfall might be underestimated or completely missed, if the snow cloud is shallow. The opposite extreme of snowfall overestimation would be snowfall that is detected at the top of the blind zone but completely sublimates on its way down to the surface. Besides these extreme scenarios, the snowfall properties observed at the top of the blind zone might also

be altered within the blind zone due to microphysical processes or wind shear. For mid-latitude systems, a general increase of the radar reflectivity factor toward the ground in the range of 3 to 7 dB/km^{-1} was found and has been associated to aggregation and depositional growth. While there is large variability, reflectivity gradients are found to generally increase with higher temperatures. [15] and [16] studied ground-based radar data for the Canadian Arctic region and found radar reflectivity in the lowest 2km above ground to be nearly constant. However, some cases revealed increasing as well as decreasing radar reflectivities in the range of 5 dB/km^{-1} toward the ground depending on the thermodynamic structure of the lowest layers and the intensity of snowfall.
To obtain the resolution for the phenomena that will be observed by the WIVERN mission with a high degree of precision, it is essential to go as far as possible to illuminate this blind zone.
For this reason, the development of the simulator can be useful in that, knowing the reflectivity profile of the specific territory over which the radar is making its measurements, it would be possible to separate the contribution due to clutter from the received return signal, thus reducing rather than eliminating the blind zone, and thus obtaining a much more accurate measurement of the phenomenon, and also making it possible to define one of the most important parameter for terrestrial observation, the Signal to Noise Ratio. Knowledge of such a parameter would enable a breakthrough in the study of phenomena characteristic of areas with complex topography, as in the case of Orographic Enhancement.
Orographic Enhancement is an intriguing meteorological phenomenon that emerges when moist air masses collide with the presence of topographic formations, such as mountain ranges. This process is triggered by the forced ascent of moist air when it encounters geographical barriers, resulting in a peculiar meteorological event.
Orographic ascent is at the heart of this phenomenon, a process in which moist air currents are forced to rise above the topography of the terrain. As the air rises, it undergoes adiabatic cooling, leading to condensation of the moisture present and increased precipitation, as shown in Figure 1.2. This increase in precipitation is what we had called aOrographic Enhancement, and its manifestation is most evident on the windward side of the mountain range. On this side, precipitation can reach significantly higher levels than in the surrounding areas, creating peculiar climatic conditions. However, on the leeward side of the mountain range, an opposite phenomenon called 'rain shadow' can be observed. Here, the descending air significantly reduces precipitation, creating a drier area that is less affected by moist air currents.
The phenomenon is a key element for meteorologists and climatologists trying to understand regional climate patterns. The analysis of this phenomenon provides a unique window to explore the complex interplay between topography and local meteorological conditions, contributing to our understanding of atmospheric processes

and their impacts on precipitation distribution and the surrounding environment. The development of the high-precision simulator be very useful in understanding these phenomena through the possibility of obtaining meteorological observations without the contribution of clutter but at the same time contextualized in areas with a very particular orography such as mountain ranges, thus enabling the phenomenon to be better analyzed also in terms of climate change, given that significant changes of precipitation are expected in the changing climate and orographic effects are important in determining the amount of rainfall at a given location. It thus becomes particularly important to understand how orographic precipitation responds to global warming and to anthropogenic forcing.

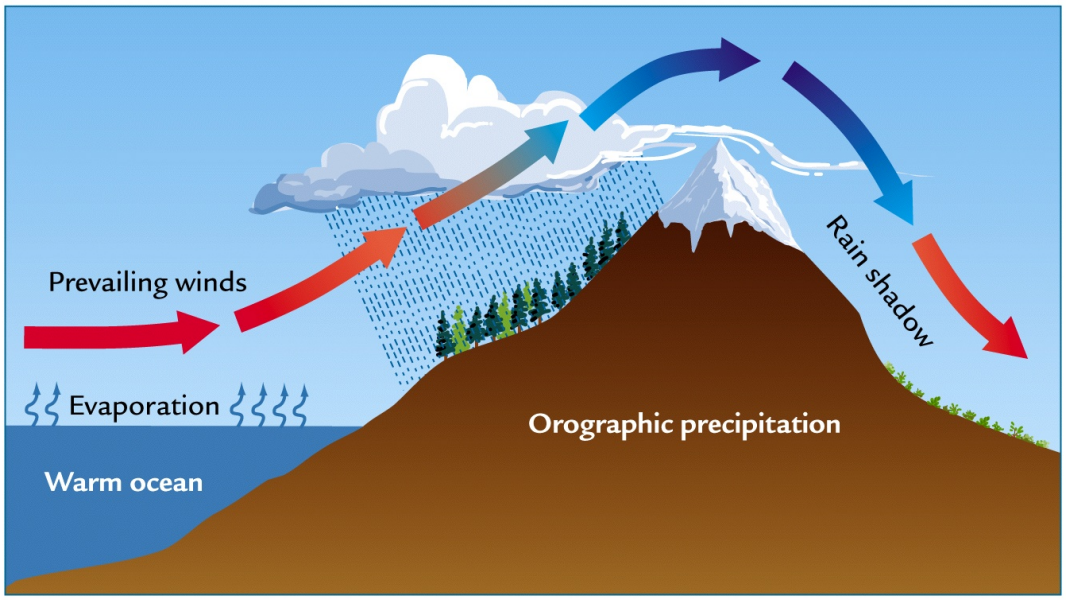

Figure 1.2: Orographic Enhancement [17]

Doppler calibration

Mispointing error refers to the discrepancy between the correct direction of radar observation and the direction to which the radar is pointed. This type of error can significantly affect Doppler measurements made by the radar, especially in applications such as atmospheric radars with conical scanning, as in the WIVERN mission. It can be caused by a variety of factors, including inaccuracies in the calibration of the radar antenna or the control of its direction, as well as dynamic effects during radar motion, and can lead to distortions in the Doppler data collected by the radar, compromising the accuracy of measurements of wind and other atmospheric

variables.
Reflectivity-weighted Doppler velocity can calibrate Doppler data, mainly when flat, immobile surfaces are involved. This is because surface reflectivity profiles are independent of azimuth scan angle, and Doppler profiles depend on scan angle. Under the assumption of a flat, immobile homogeneous surface (i.e., a constant backscattering cross-section over the entire area), at a side view, the Doppler velocity of the surface is expected to have a value of 0 m/s at all heights. In contrast, at other azimuth angles, positive and negative Doppler velocities are expected above and below the surface with 0 m/s only at the surface height. This is the result of the different orientation of the constant Doppler displacement lines induced by the spacecraft velocity compared with the lines with constant range from the radar [11].
When surfaces are no longer flat and with a (RCS) non-constant, two main problems emerge. First, variations in the reflectivity of surfaces can be significant in different areas, and these variations introduce uncertainties into the reflectivity-weighted Doppler velocity estimation due to the phenomenon of nonuniform beam filling affecting the accuracy of measurements. Second, irregular topography and nonuniform surface shapes can cause distortions in the radar observation geometry. This affects the relationship between radar target position and Doppler measurement. Distortions in the observation geometry can lead to errors in Doppler velocity estimation and, consequently, in the calibration of Doppler data, further compromising the accuracy of measurements.
The development of a simulator that takes into account these additional complexities could be very helpful in developing such a calibration method.

1.2 Thesis structure

After this first introductory **chapter 1**, the thesis is structured as follow:

- **chapter 2** presents the theoretical background. In particular:
  - The radar equation is analyzed, whcih describes radar signal power received from reflective surfaces, considering factors like transmitted power, antenna gains, wavelength, distance, and backscattering cross-section. Integration over surface area yields total reflected power.
  - Backscattering Cross-Section σ_0 measures target scattering intensity and depends on shape, dielectric constant, and incident wave parameters. Statistical properties are modeled using the random facet approach.
  - Terrain types are classified into major categories like barren land, vegetation, urban areas, and snow cover, with further subdivisions based on surface characteristics. MATLAB simulations analyze backscattering coefficients for different surfaces and angles.
- **chapter 3** covers radar simulation and analysis, including Digital Elevation Model (DEM) utilization, calculation of incidence angles, local slopes, Iso-range, and Iso-Doppler zones. It discusses antenna patterns, shaded area evaluation, and radar cross-sections, providing insights into radar signal interactions with terrain and target distributions, explaining the different steps that have been followed, the code, and the results obtained.
- **chapter 4** collects the results about this thesis.
- **chapter 5** contains a summary of the different research activities possible.

Chapter 2

Theoretical Background

In this chapter, we delve into the fundamental principles underpinning radar systems and their interaction with the environment. Beginning with an introduction on Pulse Doppler Radar and Doppler Effect, we then discuss a comprehensive analysis of the radar equation, exploring the intricate relationship between transmitted power, antenna characteristics, wavelength, distance, and backscattering cross-section. Through rigorous examination and integration over surface areas, we gain insight into the total reflected power, essential for understanding radar performance. We then delve into Backscattering Cross-Section (σ_0), Orography, and Terrain Types, providing essential theoretical groundwork for understanding radar technology.

Pulse Doppler Radar

Remote sensing is a scientific and technological discipline that deals with acquiring information and data on objects or phenomena on Earth without any direct physical contact. This methodology is based on the use of sensors placed on airborne platforms (satellites, aircraft) or on the ground, which record the characteristics of objects by receiving electromagnetic radiation emitted or reflected by them.
The main objective of remote sensing is to obtain detailed information on the Earth's surface, whether it relates to the ground, vegetation, bodies of water, or other atmospheric and geological phenomena.
Radar, which stands for '**Radio Detection and Ranging**,' is a critical technology in remote observation, meteorology, defense, and numerous other scientific and industrial applications. This instrument exploits the properties of electromagnetic waves to detect, locate, and track distant objects, making it a crucial tool in Earth observation. Radar operation is based on the principles of sending pulses of electromagnetic waves and then measuring the time it takes for them to return after interacting with a target. An example is reported in Figure 2.1. Data on the position, distance, speed, and other properties of target objects can be obtained by

analyzing this information. In the specific case of the WIVERN mission has been chosen a pulse Doppler Radar.

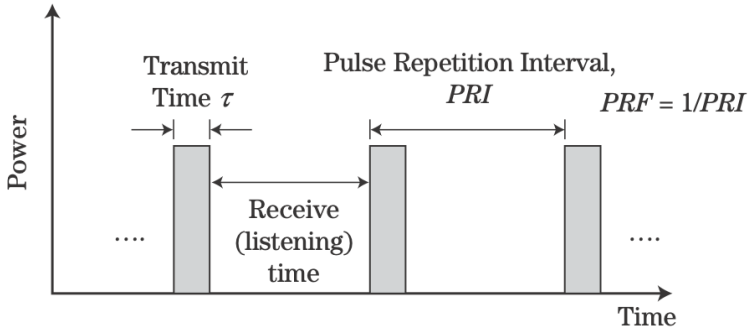

Figure 2.1: Diagram illustrating the operation of a pulsed radar system,in which listening period, combined with the pulse width, forms one complete cycle of pulsed radar operation.[18]

Doppler radar is a type of radar particularly used to measure the relative speed of a moving object relative to the radar itself. This instrument is of particular importance in atmospheric wind monitoring, where accurate measurement of wind speed is essential for a wide range of applications, from weather forecasting to flight and navigation operations. Doppler radar exploits the fundamental principle of the Doppler effect, which describes the change in the frequency of a wave when the source or observer moves relative to each other. In the case of Doppler radar, this change in the frequency of the reflected radar signal is proportional to the relative speed of the moving object relative to the radar. This means that by accurately measuring the change in the frequency of the reflected signal, the speed of the moving object can be accurately calculated.
The operation of Doppler radar is based on sending pulses of high-frequency electromagnetic energy toward the moving target, such as moving air particles within an air mass. When these pulses hit the target and are reflected back to the radar, the frequency of the reflected signal is different from the frequency of the transmitted signal due to the relative motion between the target and the radar. By measuring this change in the frequency of the reflected signal, the atmospheric wind speed can be accurately determined.
The second feature of the apparatus is pulsed operation in fact Radar waveforms can be categorized into two main types: **continuous wave** (CW) and **pulsed**. In a CW radar, the transmitter continuously emits a signal without interruption while the receiver operates continuously as well. Since a CW radar constantly transmits, determining the round-trip time of the electromagnetic (EM) wave and,

consequently, the target range, requires modifying the waveform characteristics, such as through frequency modulation.
On the other hand, a pulsed waveform radar emits pulses of finite duration separated by periods when the transmitter is inactive. These pulses are transmitted for a short duration, known as the pulse width (in WIVERN case, 3.3 μs). During this time, the receiver is disconnected from the antenna, or "blanked", to protect its sensitive components from the transmitter's high-power EM waves, and no received signals are detected. Between transmitted pulses, the receiver reconnects to the antenna, enabling it to receive any echoes reflected from objects in the environment. This listening period, along with the pulse width, constitutes one cycle of pulsed radar operation, commonly referred to as the interpulse period (IPP) or pulse repetition interval (PRI).[18]
Moreover Radars operate at different frequencies, or bands, of electromagnetic waves. The choice of band affects the radar's ability to penetrate the atmosphere and interact with different types of targets. For example, the microwave (GHz) bands are particularly effective in penetrating the atmosphere and providing high-resolution detail.
The Earth's atmosphere can hinder the propagation of electromagnetic waves. This shielding, which has made possible the development of life on the planet because organic matter is particularly fragile when hit by ionizing radiation such as UV, becomes an obstacle for remote sensing as it can affect the ability of a radar to detect and identify objects. Some frequency bands, such as microwaves, are less sensitive to atmospheric effects and are therefore ideal for atmospheric and meteorological monitoring applications.
The use of radars operating at a frequency of 94 GHz for wind monitoring represents a significant application in radar technology, with significant advantages in atmospheric observations.

The 94 GHz frequency, in the millimeter wave (mmW) band, offers high spatial resolution, enabling the detection of small-scale wind variations, such as vortices and turbulence. Millimetre waves interact with atmospheric particles, such as water droplets and aerosols, producing scattering effects that allow radars to detect the presence and movement of air.

The ability to penetrate through precipitation and clouds is a crucial aspect, as it allows winds to be monitored even in adverse weather conditions, enhancing atmospheric observation. This feature is particularly useful in meteorological applications, contributing to weather forecasting and understanding atmospheric patterns. Radars at 94GHz can offer detailed information on atmospheric structure and dynamics, improving the accuracy of weather forecasting. Furthermore, their ability to detect extreme weather phenomena, such as tornadoes and microbursts, makes them essential for early warnings and the management of weather-related emergencies.

In conclusion, the use of 94GHz radars in wind monitoring represents a significant step in the advancement of atmospheric observation capabilities, contributing to a better understanding of atmospheric dynamics and weather risk management, this justifies the choice of the WIVERN mission to use this particular wavelength for its radar sampling signal.

Doppler effect and Doppler shift

The Doppler Effect, named after the Austrian physicist Christian Doppler who first proposed it in 1842, is a fundamental phenomenon observed in waves, including sound waves, light waves, and electromagnetic waves. At its core, the Doppler Effect describes the change in frequency or wavelength of a wave perceived by an observer due to the relative motion between the source of the wave and the observer. This effect is commonly experienced in everyday life, such as the change in pitch of a siren as an ambulance passes by or the shifting of the sound of a train's whistle as it approaches and then moves away.
The Doppler Effect is based on the principle that the relative motion between the source of a wave and the observer alters the effective propagation distance of each wavefront. When the source and observer are moving closer together, the waves become compressed, resulting in an apparent increase in frequency and a higher pitch. Conversely, when the source and observer are moving apart, the waves become stretched out, leading to a decrease in frequency and a lower pitch.
The Doppler frequency shift, fd, or "Doppler" for short, is the difference between the frequency of the received wave and that of the transmitted wave and is approximately given by:

$$f_d \simeq \frac{2V_r}{\lambda}$$

the term V_r represents the radial component of the target's velocity vector in the direction towards the radar, while λ denotes the wavelength of the transmitted electromagnetic (EM) wave. This approximation holds well when the radial velocity of the target is significantly lower than the speed of light. The negative of the radial velocity, often referred to as the "range rate," indicates the speed of approach or recession of the target relative to the radar. A positive radial velocity component, and consequently a positive f_d, signifies targets moving towards the radar, whereas a negative radial velocity, resulting in a negative f_d, indicates targets moving away from the radar.
As already explained, this phase change is critical for acquiring data on the relative velocities of the surface with respect to the motion of the satellite, so that targeting analysis based on this data is possible.

2.1 Radar equation

The radar equation in the case of surfaces is a specific formulation of the radar equation that describes the signal strength received by a radar antenna. It is evaluated when the signal is reflected by a surface. This equation is fundamental in the field of pulsed-radar and radar-remote sensing, where radar waves' reflectivity (or backscattering) of a surface must be measured.

The general form of the radar equation for surfaces is given by Equation 2.1.

$$P_r = \frac{P_t \cdot \lambda^2 \cdot G_t(\phi, \psi) \cdot G_r(\phi, \psi) \cdot \sigma_0(\theta)}{(4\pi)^3 \cdot R^4} \cdot A_{eff}(\beta) \tag{2.1}$$

This formula is used to calculate the power of the radar signal received from a reflective surface. As mentioned before, this information is crucial in radar remote sensing to measure and characterize the reflectivity of different surfaces, such as land, oceans, man-made structures, and other objects. The knowledge of the received signal strength allows the radar response of surfaces to be understood and analyzed, providing useful information in various contexts.
Its constituent elements are:

- **Transmitted power** (P_t): represents the power of the radar pulse transmitted by the antenna. Its intensity is determined by the radar pulse generation system.

- **Transmitting Antenna Gain** (G_t): represents the efficiency of the antenna in concentrating the transmitted power in a specific direction. and indicates the directionality of the antenna, being a measure of signal focusing. This can be influenced by the geometry and construction characteristics of the antenna.

- **Receiving Antenna Gain** (G_r): represents the efficiency of the antenna in collecting the radar signal reflected from the surface and similarly to the gain of the transmitting antenna, a higher gain of the receiving antenna indicates a higher sensitivity in collecting the reflected signal. Being indices of directionality, both G_r and G_t are a function of azimuth angle and elevation angle

- **Wavelength**(λ): physical characteristic of the electromagnetic pulse, it is inversely proportional to the frequency of the radar signal, and is determined by the characteristics of the system. It influences the spatial resolution, according to Rayleigh's law, and the ability to penetrate through the reflecting surface. Shorter wavelengths offer greater spatial resolution but may be more prone to atmospheric absorption.

- **Distance between Antenna and Reflecting Surface** (R): this is the physical measure of the separation between the radar and the reflecting surface.
- **Backscattering Cross-Section per unit area** (σ_0): also known as Radar Cross-Section, it's a measure of how effectively a surface reflects radar waves.is a very complex parameter that depends on various factors such as shape, size, angle of incidence, and pulse frequency, as well as the composition of the reflecting surface. Because of this complexity, the study of RCS will be explored in a separate section of this chapter, but it will be treated as dependent on the angle of incidence within a pixel at fixed terrain characteristics.
- **Effective Area** (A_{eff}) : derived from the base area of the individual pixel, which is related to the spatial resolution of the DEM, and which has dimensions of 21.9×30.8 [m^2], divided by the $cos(\beta)$ factor, where beta is the local slope of the area to the flat surface, and which therefore takes into account the orientation of each pixel concerning the direction of the antenna signal.

Radar equation formulation is the result of two contributions:

1. one related to the propagation of the wave from the radar to the surface;
2. one related to the propagation of the reflected wave, thus from the surface to the radar.

Assuming that electromagnetic waves propagate under ideal conditions when high-frequency energy is radiated by an isotropic antenna, it propagates uniformly in all directions.
Areas of equal power density then form concentric spherical surfaces ($A = 4\pi R^2$) around the antenna. As the radius of the sphere increases, the same amount of energy disperses over a more spherical area. This means that the power density, in a given direction, decreases as the distance from the transmitter increases given a certain transmitted power P_t at a given distance R_1 from the observed surface, the transmitted power density is called S_{omni}, for an isotropic antenna:

$$S_{omni} = \frac{P_t}{4\pi \cdot R_1^2} \tag{2.2}$$

In reality, the antenna only transmits over part of the sphere (for a constant transmission power), ergo the power density increases in the direction of transmission. This characteristic is precisely the antenna gain defined above. This gain is due to the concentration of the transmitted power in one direction. Then the formula for calculating the power density in the direction of maximum gain will become:

$$S_{conc} = S_{omni} \cdot G = \frac{P_t}{4\pi R_1^2} \cdot G \tag{2.3}$$

Reiterating that we are going to ignore transmission losses and atmospheric disturbances, the observed surface will then be invested by the concentrated power density based on the directionality of the antenna and will reflect a part of it, which we call P_{refl}.
To determine the value of this useful reflected power, it is necessary to know the RCS of the target. The value of *sigma*, dependent on many parameters, weighs the amount of power returning from the target towards the source of the electromagnetic pulse. It should be specified that in this case, the *sigma* values are not per unit area because integration has not yet occurred.
Therefore, the reflected power Pr is the result of the power density s_{omni}, the antenna gain G, and the highly fluctuating radar cross-section σ:

$$P_{refl} = \frac{P_t}{4\pi R_1^2} \cdot G \cdot \sigma \tag{2.4}$$

considering the observed surface as a transmitter sending an amount of power equal to Pref, with the same signal propagation conditions, we can define the power density transmitted by the surface and received by the source as:

$$S_{refl} = \frac{P_{refl}}{4\pi \cdot R_2^2} \tag{2.5}$$

The total energy received by the antenna is dependent on the geometric aperture of the radar A[m^2] reduced by an efficiency factor K_a, whose value is normally between 0.6 and 0.7.
We can therefore define the received power P_r as:

$$P_r = S_{refl} \cdot A \cdot K_a \tag{2.6}$$

and again,with a series of mathematical steps, expressing the reflected power density and substituting the reflected power with its extended formula we obtain:

$$P_r = \frac{P_{refl}}{4\pi \cdot R_2^2} \cdot A \cdot K_a \tag{2.7}$$

$$P_r = \frac{\frac{P_t}{4\pi R_1^2} \cdot G \cdot \sigma}{4\pi \cdot R_2^2} \cdot A \cdot K_a \tag{2.8}$$

Finally, we can relate the effective aperture of the radar to the gain and wavelength of the electromagnetic pulse using the expression:

$$A \cdot K_a = \frac{G \cdot \lambda^2}{4\pi} \tag{2.9}$$

and substituting in (2.8), considering the simplification $R_2 = R_1 = R$, we obtain the radar equation for surfaces (2.1) defined at the beginning of the section:

$$P_r = \frac{P_t \cdot G_t \cdot G_r \cdot \lambda^2 \cdot \sigma}{(4\pi)^3 \cdot R^4}$$

The equation describes the return signal in terms of power for any concentrated target, but since one of the main objectives of the work is to obtain is the return profile of the power reflected from the entire orographic surface being observed in such a way as to go to extrapolate with high accuracy the amount of return signal due to ground clutter from the total return, formed altogether by the contribution of the signal mentioned earlier plus that of the signal from the hydrometeor that is being observed, thus obtaining for the latter data with a degree of accuracy entirely new for today's observations.
An integral of the surface is thus made to equation (2.1), and this integration concerning the reflecting area returns the total power reflected by the entire surface. The integration of the equation can be represented as follows:

$$P_r = \frac{P_t \cdot \lambda^2}{(4\pi)^3} \cdot \int_S \frac{G_t \cdot G_r \cdot \sigma}{R^4} \, dA \tag{2.10}$$

and the result is the total power reflected from the entire surface. This is particularly useful when assessing the ability to detect an entire reflective structure or surface, such as an orographic surface. It should be noted that through this pathway integration step, the RCS becomes per unit area $\sigma_0 = \frac{\sigma}{A}$.
The contribution of each individual pixel to the total power reflected from the surface can be expressed as:

$$P_r^i = \frac{P_t \cdot G_i^2 \cdot \lambda^2 \cdot \sigma_{0_i}}{(4\pi)^3 \cdot R_i^4} \cdot A_{eff} \tag{2.11}$$

where the infinitesimal area dA is replaced by the effective area $A_{eff}(\beta)$, defined at the beginning of the section. An example is reported in Figure 2.2.

$$A_{eff} = \frac{\Delta x \cdot \Delta y}{cos(\beta_i)}$$

should be specified again that the subscript i indicates that those specific quantities vary among the various discretized points in the DEM.
By discreteising the domain of integrations into n

$$P_{r_i} = \frac{P_t \cdot \lambda^2}{(4\pi)^3} \cdot dA \sum_{i=1}^{n} \frac{G_{i^2} \cdot \sigma_{0_i} \cdot A_{eff}}{R_{i^4}} \tag{2.12}$$

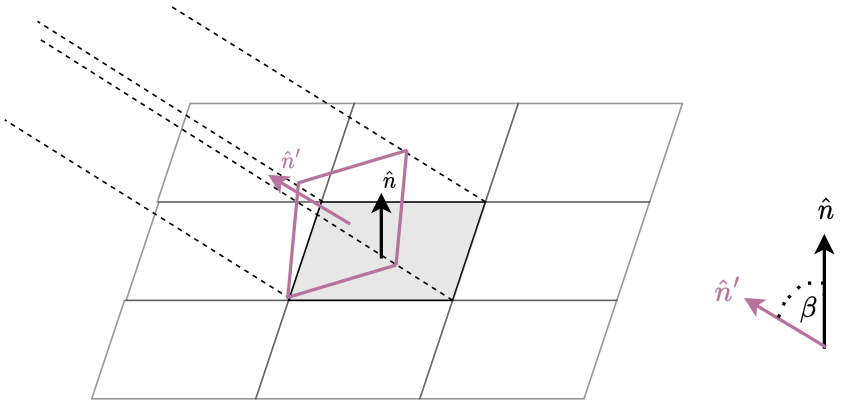

Figure 2.2: Projected Area

By calculating the Pr contribution for all the zones at a given range,the reflected power profile of the entire scene will be obtained. Therefore, when calculating the reflected power Pr , which represents the total power reflected by the entire surface, the contribution of each area element dA on the reflecting surface is already taken into account. This is especially relevant when dealing with complex surfaces, such as orographic surfaces. In real environments, surfaces may have irregular shapes and variations in reflectivity at different points.
The parameters that are within the summation, are all those variable parameters within the single pixel of the source DEM that depend on the analyzed subarea that belongs to a single ranger interval are specifically antenna gain ,the distance of the points contained in that interval and the RCS of the pixel.

2.2 Backscattering cross-section σ_0

2.2.1 Physics Derivation and Characteristics

The radar cross-section σ, denominated in units of area, serves as a parameter characterizing the scattering "intensity" of a target, particularly in the context of backscattering. This parameter encapsulates the effective area of the target and is intricately linked to its shape, dielectric constant, viewing geometry, as well as the wavelength and polarization orientations of both the incident and scattered electromagnetic waves. From the perspective of electromagnetic scattering theory, the conventional definition of σ establishes it as the ratio of the scattered power density S_p^s, measured at a distance R from the scatterer, to the power density S_q^i of an incident plane wave:

$$\sigma_{pq} = \lim_{R\to\infty}(4\pi R^2 \cdot \frac{S_p^s}{S_q^i}) \tag{2.13}$$

This definition underscores the fundamental role σ of in quantifying the target's interaction with incident waves, providing insights into the target's scattering characteristics under varied electromagnetic conditions.

It is specified the limit to infinite to denote the far field regions of the observation point.Moreover the far field power density S_p^s is function of R^{-2} ,which makes σ_{pq} independent of R,as it should be.
The subscripts q and p denote the polarization directions of the incident and scattered waves, respectively. When the earth's surface is used as a reference plane, it is often convenient to use the orthogonal pair of linear polarizations known as horizontal and vertical to describe the direction of the electric field.
For the configuration shown in figure , the reference plane is the x-y plane, the propagation direction of the incident wave is $\hat{k_i}$; and that of the scattered wave is $\hat{k_s}$,. The electric field vector of the incident wave can be expressed as:

$$E^i = E_h^i \cdot \hat{h_i} + E_v^i \cdot \hat{v_i} \tag{2.14}$$

where E_h and E_v are the vertical and horizontal polarized components of E^i and $\hat{h_i}$ and $\hat{v_i}$ are unit vectors defined by:

$$\hat{h_i} = \frac{\hat{z} \times \hat{k_i}}{|\hat{z} \times \hat{k_i}|} = xsin(\phi_i) - ycos(\phi_i)$$

and

$$\hat{v_i} = \hat{k_i} \times \hat{h_i} = -xcos(\phi_i)cos(\theta_i) - ycos(\theta_i)sin(\phi_i) + zsin(\theta_i)$$

For the scattered field:

$$E^s = E_h^s \cdot \hat{h}_i + E_v^s \cdot \hat{v_s} \tag{2.15}$$

the polarization vectors may be defined relative to $\hat{k_s}$, the propagation direction of the scattering wave, or relative to$\hat{K_r} = -\hat{k_s}$ the unit vector pointing from the receive antenna towards the scatterer.
The latter approach is more convenient in practice because the polarization vectors

$$\hat{h_s} = \frac{\hat{z} \times \hat{k_r}}{|\hat{z} \times \hat{k_s}|} = xsin(\phi_s) - ycos(\phi_s)$$

and

$$\hat{v_s} = \hat{k_r} \times \hat{h_s} = -xcos(\phi_s)cos(\theta_s) - ycos(\theta_s)sin(\phi_s) + zsin(\theta_s)$$

assume the same form as $\hat{h_i}$ and $\hat{v_i}$,and in backscattering case ($\sigma_i = \sigma_s$ and $\phi_i = \phi_s$), the two pairs of versors become identical. Figure 2.3 shows the context just described.

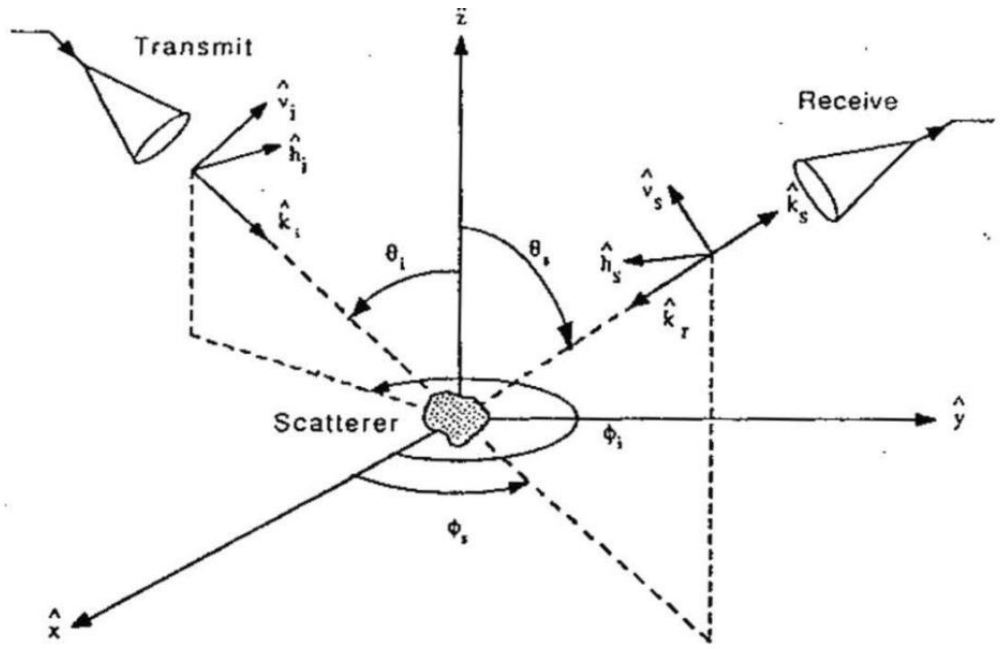

Figure 2.3: Scattering geometry. [19]

Returning to Equation 2.13, the *hh*-polarized and *vh*-polarized backscattering cross section are given by:

$$\sigma_{hh} = \lim_{R\to\infty}(4\pi R^2 \cdot \frac{E_h^{s\,2}}{E_h^{i\,2}}) \tag{2.16}$$

$$\sigma_{vh} = \lim_{R\to\infty}(4\pi R^2 \cdot \frac{E_v^{s\,2}}{E_h^{i\,2}}) \tag{2.17}$$

where it has been used the relation:

$$S_q = \frac{E_q^2}{\eta}$$

for the power densities of both the incident and scattered waves.
The quantity η is the intrinsic impedance of the medium, which in this case is air. Definition similar to the two equations above may be written for σ_{vv} and σ_{hv}.In the backscattering direction, the scattering process is reciprocal, which leads to the equality:

$$\sigma_{hv} = \sigma_{vh}$$

The cross sections σ_{vv} and σ_{hh} are called the like-polarized components, whereas σ_{vh} and σ_{hv} are called the cross-polarized or depolarized components because they are generated as a result of a change in the direction of the electric field (of the incident wave) upon scattering by the target. In practice, σ_{hh} and σ_{vh} are measured as a pair by using an h-polarized transmitting antenna and a two-channel dual-polarized receiving antenna.
If the transmitting antenna polarization is switched to v, the receive antenna will measure σ_{vv} and σ_{hv}.

2.2.2 Statistical proprieties of distributed targets

By applying the radar equation to a distributed target, one goes on to integrate this equation for a defined surface and will consequently have the transition from σ to σ_0 , which is defined as the backscattering cross-section of a distributed target of horizontal area A, normalized concerning A:

$$\sigma_{0pq} = \frac{\sigma_{pq}}{A}$$

Going to consider to a first approximation all the other terms in (2.1) constants inside each pixel, the power received due to backscatter from an illuminated area that subtends a small solid angle as viewed from the radar is directly proportional to the backscattering coefficient σ_0 , regardless of the specific type of radar used. When a flat surface is illuminated by a radar wave at oblique incidence, the wave is specularly reflected in accordance with Snell's law and no energy is scattered toward the radar. Most terrain surfaces are not flat, however, and, consequently, they scatter the incident energy in many directions, including the backscattering direction.
The directional pattern of the energy scattered by a rough surface is governed by the dielectric constant, the degree of roughness of the surface, and the parameters of the incident wave (incidence angle, wavelength, and polarization direction). Backscattering from terrain can also occur as a result of volume scattering in inhomogeneous media, such as vegetation canopies and snow cover. When illuminated by a radar beam, a distributed terrain target-be it a bareground surface or a ground surface covered with a layer of another material is usually modeled as an ensemble of scattering centers randomly distributed in spatial position over the illuminated area (or volume).
One of the simplest models used to characterize a rough surface,and which in particular is used for this discussion,is the random facet model. The rough surface is approximated through a series of small planar facets, each tangential to the actual surface. The facet model treats the scattering from the assemblage of such facets by taking into account both their reradiation patterns and the distribution of their slopes. The center of each facet represents a scattering wave is a narrow-band coherent signal, the received signal is the phasor sum of the signals reradiated by all of the scattering centers located in the illuminated area. Thus, the amplitude of the received radar signal is governed not only by the strengths of the reradiated signals, but also by their locations. This means that the received signal is a random variable governed by a statistical process related to the statistical properties of the scattering centers.
In the next chapter, we shall examine the statistical characteristics of the received radar signal of seven different types of terrain.

2.2.3 Terrain types

The preceding section outlines the rationale for designing an ideal classification scheme for terrain based on the principles of phenomenology. An ideal classification scheme would incorporate all aspects of the phenomenology. The organizational structure of such a scheme would impart an understanding scattering mechanisms and permit the identification and aggregation of terrain categories that exhibit similar scattering behaviors. From a strictly phenomenological perspective, a logical structure might utilize a top down description of terrain from the sensor viewpoint wherein terrain would be classified by the presence and nature of intervening media (such as snow and vegetation) and subclassified by the nature of the underlying substrate with respect to roughness and dielectric properties. Although such an approach is valid from the standpoint of the scattering mechanisms, it is not consistent with the traditional terrain classification scheme.
Terrain is initially subdivided into four major categories: barren and sparsely vegetated land, vegetated land, urban land, and snow-covered land. Open water surfaces (such as lakes and rivers) and ice are excluded from treatment. However, because the state of water (liquid or frozen) as contained in snow, soils, and vegetation is a prime determinant of dielectric properties, all data are annotated as to the thermal regime at the time of observation. Each of the major categories is further subdivided based on surface roughness, vegetation class, land use, and near-surface dielectric properties.

Number	**Name**
1	Soil and rock surfaces
2	Trees
3	Grasses
4	Shrubs
5	Short vegetation
6	Road surfaces
7	Dry snow
8	Wet snow

Table 2.1: Categories in the database

The database is organized according to the categories described in Table 2.1: Soil and rock surfaces, trees, (3) grasses, (4) shrubs, (5) short vegetation, (6) road surfaces, (8) dry snow, and (9) wet snow. This categorization reflects the hierarchical organization discussed, with each category representing a specific aspect of terrain phenomenology and scattering behavior.

A MATLAB code generates a plot visualizing backscattering coefficients for the various surface types at different angles. Initially, custom colors are defined in RGB format for later use in the plot. Two arrays, `valid_strings` and `elements`, hold labels for surface types and their corresponding descriptions. Cell arrays are initialized to store angle vectors and backscattering coefficients for each surface type. A loop iterates over each surface type. Within the loop:

- The `plot_sigma()` function is called with the current surface type to obtain angle and coefficient data.
- Retrieved data is stored in the corresponding cell arrays.

Once all data is collected, the plot is generated. For each surface type confidence intervals are calculated based on the standard deviatio, and depending on the frequency band, data is plotted with or without dashed lines. Moreover, each surface type's data is plotted using its defined color. The finalized plot provides insights into how backscattering coefficients vary across different materials and angles, crucial for remote sensing and radar applications. The final results is shown in Figure 2.4.

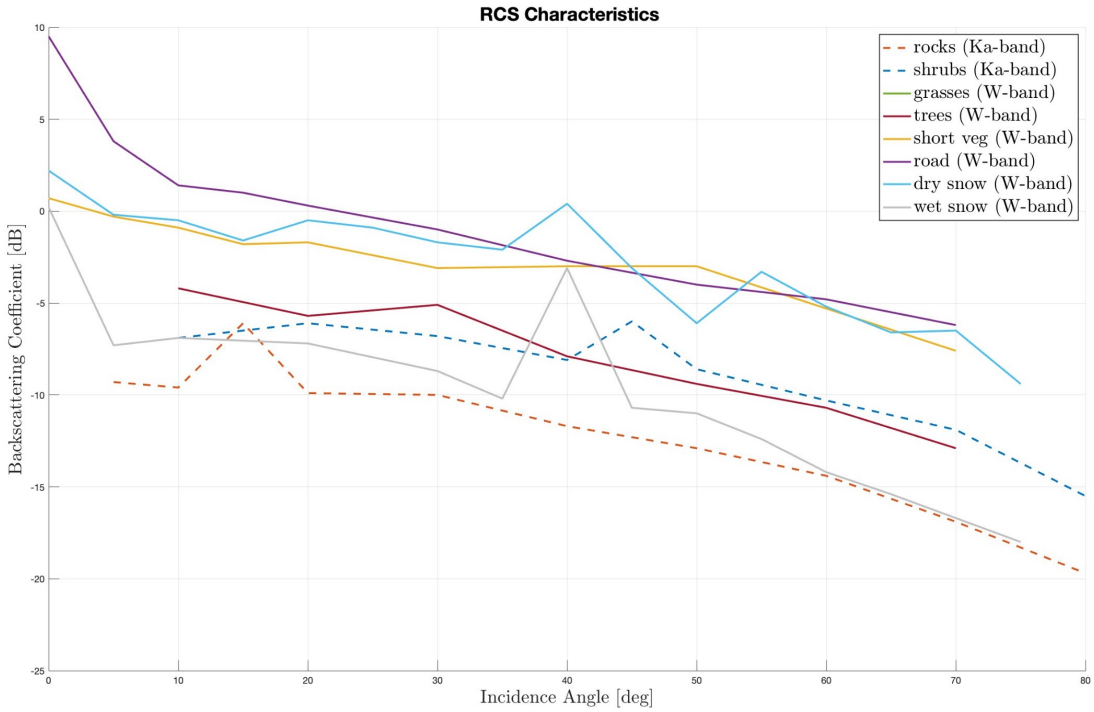

Figure 2.4: RCS Characterization

In statistics, percentiles are a way to divide data into equal parts. The k-th percentile represents the value below which k% of the data points fall. For example, the 50-th percentile is the median, dividing the data into two equal halves. Percentiles help understand the distribution of data and identify extreme values.

Standard deviation, on the other hand, measures the dispersion or spread of data points around the mean. It quantifies how much the values in a dataset deviate from the mean value. A higher standard deviation indicates greater variability within the dataset. This part of the MATLAB simulator primarily concerned with analyzing radar measurements of backscattering coefficients and Linear Depolarization Ratio (LDR) for various surface types at specific angles of incidence. It begins by defining two variables, which determine the surface type and the specific parameter being analyzed (e.g., backscattering coefficients), and the angle of incidence, respectively. Next, a function compute interpolated sigma values based on the given parameters.

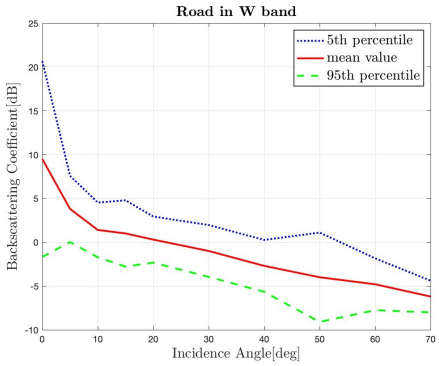

(a) Road

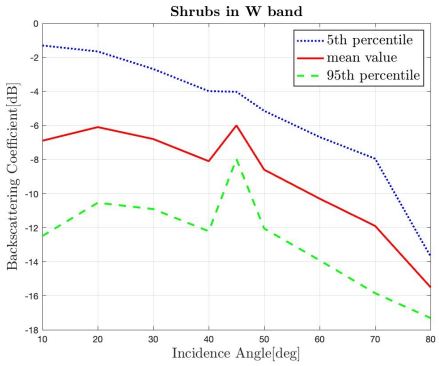

(b) Shrubs

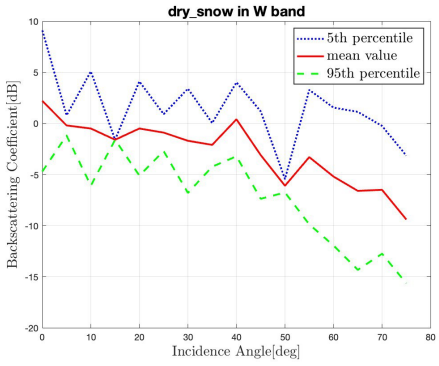

(c) Dry Snow

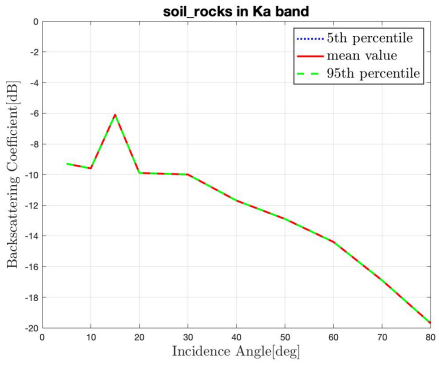

(d) Soil Rocks

Figure 2.5: Trend of the RCS function as a function of the angle of incidence with percentiles.

These sigma values are essential for understanding the radar behavior concerning different surface properties and angles of incidence. The code then proceeds to generate plots to visualize the behavior of backscattering coefficients and LDR. It calculates the 5th and 95th percentiles based on the mean value and standard deviation of the data. These percentiles offer insights into the variability and spread of the data points. If the data for horizontal polarization is available, indicating the presence of LDR measurements, the code plots a scatter plot for LDR values. Otherwise, it only plots the backscattering coefficients.

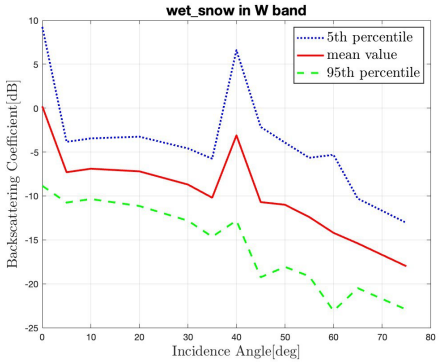

(a) Wet Snow

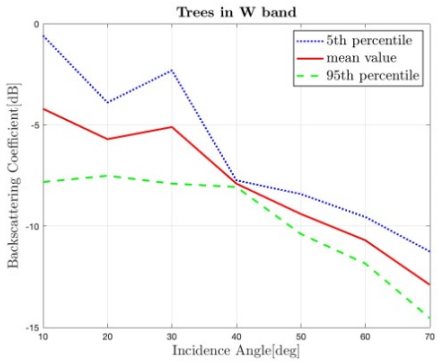

(b) Trees

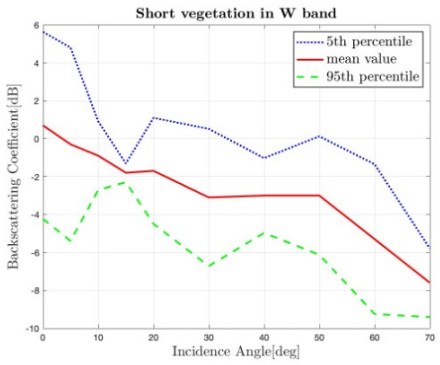

(c) Short vegetation

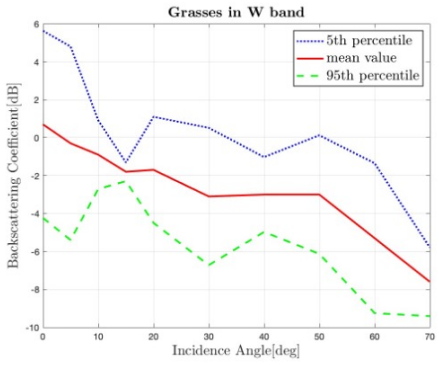

(d) Grasses

Figure 2.6: Trend of the RCS function as a function of the angle of incidence with percentiles.

The results for each categories are reported in the different subplots of Figure 2.5 and Figure 2.6. Overall, this code segment provides a statistical analysis of radar measurements, helping researchers interpret the variability and distribution of backscattering coefficients and LDR for different surface types and angles of incidence.

Chapter 3

Description of the radar clutter simulator

In this chapter we will go on to show how we were able to integrate the effect of orography into the calculation of the reflected power density from the surface,both from the point of view of surface roughness, and from the point of view of the different electromagnetic wave reflection properties of the various types of terrain. To do this we will detail all the fundamental components of the code created to go about recreating the desired results.

Orography refers to the study of terrain features such as mountains, valleys, hills, and slopes. These topographical characteristics have notable effects on radar systems, influencing signal behavior and radar performance in various ways.
The irregular terrain of mountains and valleys can cause significant deviations in radar signal propagation. When radar waves encounter terrain obstacles, they can undergo scattering, diffraction, and reflection, leading to complex signal patterns. Mountains, for example, may block radar signals, creating shadow zones or blind spots behind them. Conversely, valleys and other concave terrain features may act as waveguides, channeling radar signals and enhancing propagation over longer distances.
The other main effect caused by terrain features is obscuring or masking radar echoes from targets of interest, complicating detection and tracking. Radar systems must contend with clutter generated by ground returns from many different terrain surfaces, such as vegetation, and man-made structures. Understanding the terrain's clutter characteristics is essential for distinguishing between legitimate targets and background noise.

3.1 Power response simulator

This section delves into radar signal simulation over varied terrains. Exploring Digital Elevation Model (DEM) Code, incidence angles, and slopes, it uncovers the nuances of radar interaction. Concepts like iso-range zones, antenna patterns, shaded areas, and terrain models are dissected, offering insights into radar performance. With a focus on Radar Cross Section (RCS) analysis, this chapter provides a concise yet comprehensive guide to power response simulator that has been implemented.

3.1.1 Digital Elevation Model Code

In Listing 3.1, the MATLAB code reads and visualizes a Digital Elevation Model (DEM) from a GeoTIFF file downloaded from [20]. The site is part of the Earth Science Data Systems (ESDS) Program provides full and open access to NASA's collection of Earth science data for understanding and protecting our home planet,in which among the many data present are the ASTER files.
Aster is an Advanced Spaceborne Thermal Emission and Reflection Radiometer obtains high-resolution images of Earth in 14 different wavelengths of the electromagnetic spectrum, ranging from visible to thermal infrared light, and it contains data from almost all areas of the planet, in tiff format and divided according to latitude and longitude values. Scientists use ASTER data to create detailed maps of land surface temperature, emissivity, reflectance, and elevation. Starting from the tiff file, we extracted metadata using `geotiffinfo`, defines geographical limits, and creates a map with grid lines.
The code then displays the DEM on the map, with a color based representation of the various elevations. Let's see a little bit more details.

```
1  [~,~,~,path_MatlabShapeFiles] = PathDefinition;
2  path_MatlabShapeFiles = "dem_files";
3  tiff_file = [path_MatlabShapeFiles 'ASTGTMV003_N03W008_dem.
       tif'];
4  tiff_file = "ASTGTMV003_N45E007_dem.tif";
5  tiff_info = geotiffinfo(tiff_file);
6  [refZ,refobj] = eadgeoraster (tiff_file,'
       CoordinateSystemType','geographic');
7  zlimits=[-20 3500];
8  LaMax = refobj.LatitudeLimits(2);LoMin = refobj.
       LongitudeLimits(1);
9  LoMax = refobj.LongitudeLimits(2);
10 par_space = 0.2;
11 mer_space = 0.2;
12
```

```
refZ_sub = double(refZ);refobj_sub = refobj;

figure;
clfaxesm('Mercator','MeridianLabel','on','ParallelLabel','on
    ','MLabelParallel','south',...
     'MapLatLimit',[LaMin LaMax],'MapLonLimit',[LoMin LoMax
    ],... 'PLineLocation',LaMin:par_space:LaMax,'
    MLineLocation',LoMin:mer_space:LoMax,...
     'PlabelRound',-1,'MlabelRound',-1, ...    'LabelFormat',
     'signed', 'Grid', 'on','Gcolor','k');
framem ontightmap
geoshow(refZ_sub,refobj_sub,'DisplayType','texturemap');
    caxis(zlimits)
colormap(demcmap(zlimits));h_cb = colorbar;
h_cb.Label.String = 'Raw Elevation [m]';
```

Listing 3.1: Example MATLAB code

First, the code adds a directory to the path for MATLAB shape `geotiffinfo` reads the geographic information from a GeoTIFF file specified,in particular, the file containing data from western Piedmont, between the seventh and eighth meridians and the 45th and 46th parallels, was chosen for our case study.
The choice is justified by the fact that this is an interesting area both from an orographical point of view, with its imposing heights, but also numerous plains and hills, and for its great differentiation of soil types, ranging from wet, natural and wild areas to more urban and industrial areas..
The `geotiffinfo` function in MATLAB is used to extract metadata information from GeoTIFF files. GeoTIFF is a standard file format that allows georeferencing information (spatial metadata) to be embedded.
This spatial metadata includes details about the geographic location, coordinate system, pixel dimensions, and latitude and longitude limits of the raster data. The most important information in the GeoTIFF file is the Digital Elevation Model (DEM) data. DEM is a representation of the Earth's surface topography as a grid of elevation values, with a very high resolution of the data, in fact, we have georeferenced information with a detail of about thirty metres, contained in the various pixels that go to build the data matrix we are going to work with.

The line `tiff_info = geotiffinfo(tiff_file)` is used to read and store the metadata information of the GeoTIFF file specified by tiff_file. The returned information (tiff_info) includes details about the coordinate system, spatial referencing, data type, and other characteristics of the raster data in the GeoTIFF file.

After defining the spacing parameters for parallels (par_space) and meridians

(mer_space) in the map, the code creates subsampled data (refZ_sub) and associated geographic information (refobj_sub) for further processing. Finally, it sets up a map figure using mercator projection with specified latitude and longitude limits, grid lines, and labels.

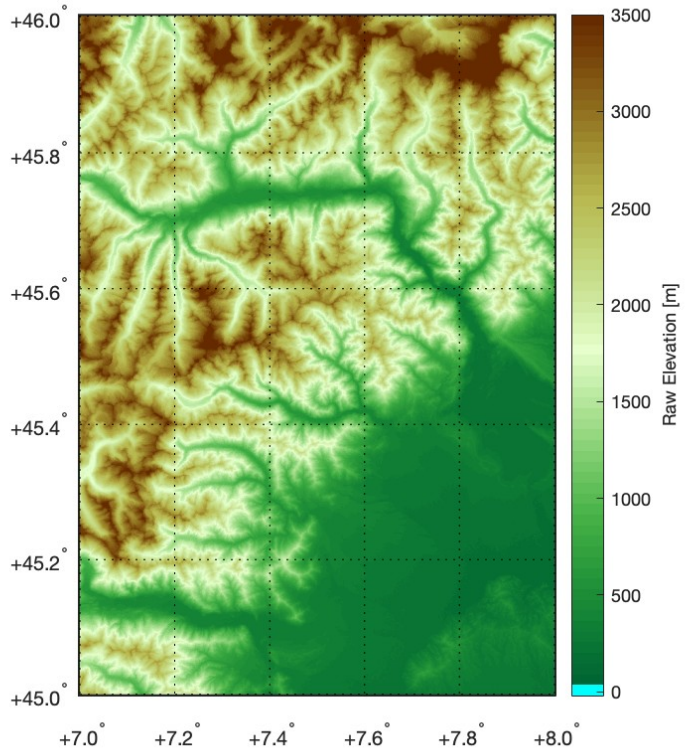

Figure 3.1: Tiff image

From the whole matrix we select a sub-area so that the contribution of each pixel in the chosen area is relevant. An example is shown in Figure 3.1.
To do this we need the size of the scene to be comparable to the beamwidth of the main beam,defined as the point where the signal power falls 3 dB below the maximum value. This value is also called Half power beamwidth since a decrease of 3 dB is equivalent to a decrease of fifty per cent in terms of power.

3.1.2 Incidence angle and Local Slopes

From the data characterizing the elevation of the chosen area it will be possible to derive numerous basic information ,such as the distance between DEM points, the distance between satellite and scene points, position versor etc., which will serve as the data base for all parts of the code that goes to make up the simulator. In this section we will describe two fundamental elements for simulation, the ray-pixel angle of incidence and the local slope.

Ray-pixel incidence

The first step, using MATLAB's `gradient` function, is to calculate the elevation gradients in the x- and y-direction of my sub-scene. Once this is done, the norm of the components is calculated, taking the third dimension into account, and with this data, the normal versor to each pixel of the desired scene can be derived.
Once this data has been obtained, the position versor at each point of the matrix is calculated by vector subtraction between the x, y and z coordinates of the points in the scene and the satellite coordinates, all in the reference system of the chosen scene. Once this subtraction has been obtained, it is normalised and the various desired position vertexes are obtained.

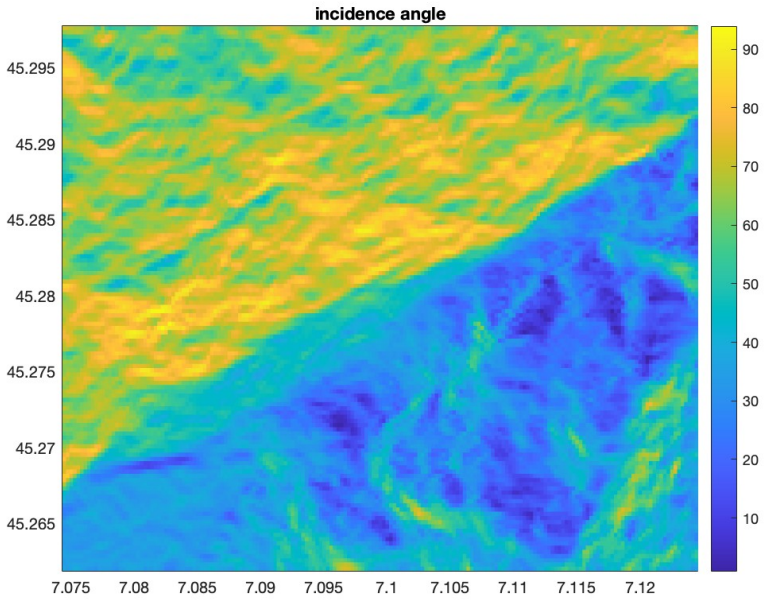

Figure 3.2: Variation of incidence angles in the scene

Thanks to these two types of versors, it is now possible to go on to calculate the

scalar product between them, so that the arcocosine of the result is then calculated, thus obtaining an angle, which we define as the angle of incidence of the beam on the orographic surface.It is important to note, as can be seen from the use of the arcocosine, that the incidence of the beam is defined as the angle inscribed between the point-satellite conjunction and the normal to the surface.
If in a scene without orography, the angle of incidence will have almost irrelevant variations, depending only on the size of the analysed area, when you go to do this calculation in a scene where you have different heights, due to the presence of more or less extreme gradients, the angle of incidence will take on very different values between the various pixels, as can be deduced from the image in Figure 3.2.

Local slopes

Local slopes refer to the steepness of the terrain at each point in the scene and are essential for determining the area by which each pixel in the sub-scene contributes to the received signal power density value
The calculation process for this variable is based on the same idea with which we derived the angle at which the pulse impinges on each pixel.Starting with the versori normal to the surface already obtained in the previous step, we calculate the scalar product with the vector normal to a generic flat surface and derive the angle that lies between the two elements.
By incorporating information about local slopes into radar simulations and analyses, researchers can improve the accuracy of terrain characterization, radar signal processing algorithms, and the interpretation of radar imagery. The area dS_{ij} then can be computed as a function of the DEM pixel area $\Delta x_i; \Delta y_j$, that are obtained from the spacing of DEM points in the longitudinal and latitudinal directions, by:

$$dS_{ij} = \frac{\Delta x_i; \Delta y_j}{\cos(\beta_{ij})}$$

where β_{ij} represents the slope of the ij surface element.

3.1.3 Iso-range and Iso-Doppler zones

In pulse-Doppler radar systems, it is useful to introduce the concept of iso-range zones and iso-Doppler zones.
Iso-range zones refer to regions of constant range or distance from the radar. Each zone represents a specific distance from the radar, allowing the radar to segment the observed area into concentric circles or spherical shells centered around the radar itself. By dividing the observed space into these iso-range zones, the radar can effectively store and analyze the returning signals based on the distance of the target from the radar.
The dimension of these zones has been chosen in accordance with the pulse of the signal, τ. In fact, to process every signals effectively, they are typically sampled at discrete time intervals using an analog-to-digital converter (ADC). This sampling quantizes the signal both in time and amplitude. The time quantization is determined by the ADC sample times, while the amplitude quantization depends on factors such as the number of ADC "bits" and the full-scale voltage. To ensure accurate detection, the time between samples must be shorter than the duration of a transmitted pulse. For instance, if the radar transmits a pulse lasting 1 microsecond, the received signal must be sampled at intervals of no more than a microsecond. To enhance detection capabilities, oversampling is often employed. For instance, the radar may take two samples within the duration of a single pulse. For a 1 microsecond pulse width, this would suggest a sample period of 0.5 microseconds, equivalent to a sample rate of 2 megasamples per second (Msps). Each of these time samples corresponds to a different range increment, commonly referred to as a "range bin". In the case of WIVERN mission,this quantity it's almost equal to a value of 125 metres. These range bins allow the radar to discretize the observed space into distinct segments, facilitating accurate target detection and tracking. To find these zones we proceeded to calculate the distances of each pixel in the scene from the satellite, subtracting the range value from the boresight so as to have values that make the study easier to read, going to group them according to the range bin described above.
An example it's shown in Figure 3.3.
As can be seen from the image, the orientation of these areas with respect to the satellite depends on the Azimuth angle of the satellite with respect to the scene it is observing.In addition, it can be seen that the lines turn out to be irregular, and the reason is related to the presence of orography in the scene, due to the differences in the elevation of the points that it entails.
Similarly, iso-Doppler zones represent regions of constant Doppler frequency shift. These zones are determined by the relative velocity of the target with respect to the radar. Each iso-Doppler zone corresponds to a specific Doppler frequency shift, indicating the velocity of the target along the radar line of sight. By identifying

these iso-Doppler zones, the radar can differentiate between targets moving towards or away from the radar, as well as determine their velocities.

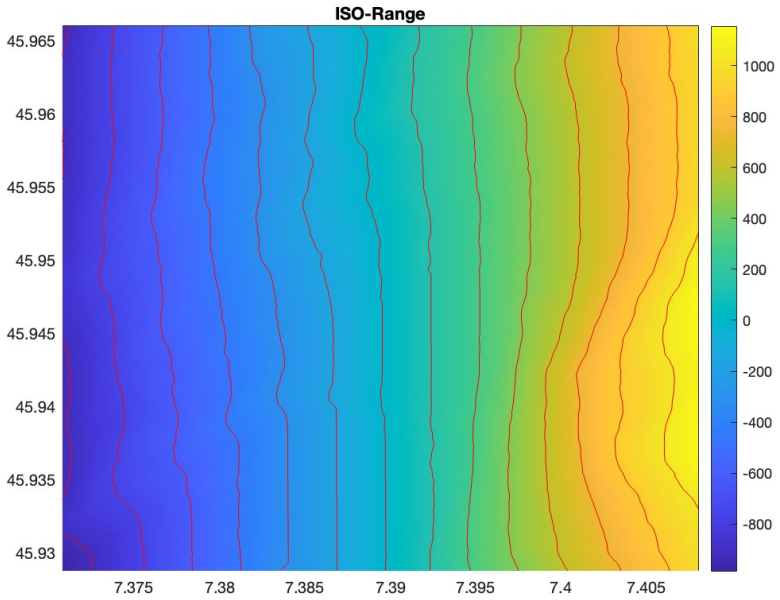

Figure 3.3: Example of isorange zones with a 125 m sampling in a *side view* ($\phi = 0$) situation

To obtain the doppler velocity,initially key parameters such as Earth's radius, mass, and gravitational constant are defined.These three parameters,with the mean of the satellite height above the surface, are essential to go to calculate the satellite's orbit velocity around the earth, also called the first cosmic velocity,using established celestial mechanics principle:

$$V_c = \sqrt{\frac{\mu}{R_E + S_z}}$$

it is understated how this was approximated to a circular orbit. The computational process iterates over each point within the scene,and for each point, a directional vector is constructed, representing the direction from the satellite to the point, normalized for consistency. A reference point is established,that once again represent the direction from the satellite to the scene's center. This serves as a rescaling factor for subsequent computations.
Doppler velocities for each scene point are computed by calculating the scalar product between the satellite's velocity vector and the normalized directional vector.

Through this step, the projection of the component of the satellite's velocity with each point's direction is generated. The last step is rescaling all the values subtracting the reference quantity at the boresight, to ensures that Doppler velocities are referenced relative to the scene's center point velocity, facilitating coherent analysis.

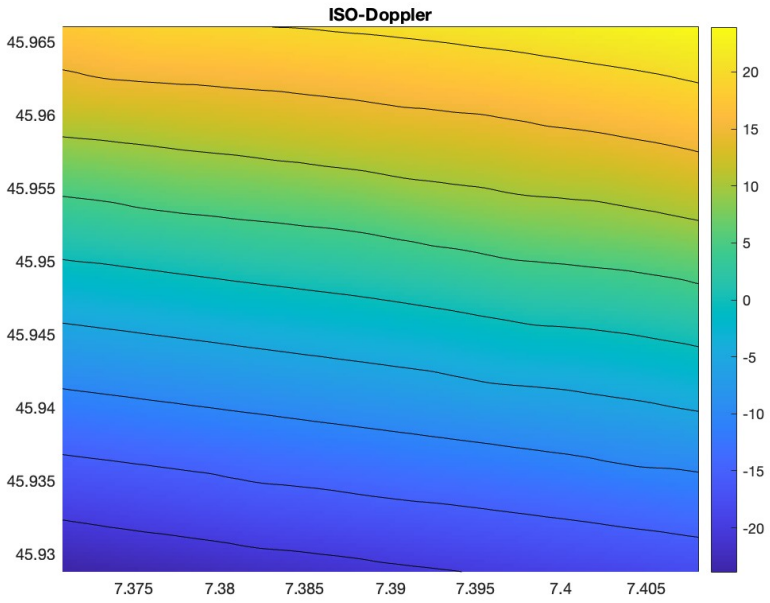

Figure 3.4: Representation of curves characterized by an equal Doppler velocity

3.1.4 Antenna Pattern

In the context of satellite systems, antennas play a vital role in transferring and receiving signals, and understanding their gain and pattern is critical to ensuring optimal performance and reliable connectivity complex, distributed networks on the right scale.
An antenna is a transducer designed to transmit and receive electromagnetic waves, that converts electromagnetic waves into electrical AC and vice versa. The apparatus itself is physically an arrangement of conductors that generate a radiating electromagnetic field in response to an applied alternating voltage and the associated alternating electric current. There are numerous configuration for this component, which differ from each other in the performance they have to provide. There are various types of antennas, each designed to suit specific transmission, reception and signal directionality requirements. Among the most common types of antennas are dipoles, which consist of a conductor divided into two equal parts, used extensively in radio and television antennas. Then there are directional antennas, known as Yagi-Uda antennas, which have a series of directional elements arranged linearly on a pylon, and are frequently found in television broadcasting and long-distance communications; parabolic antennas, characterised by a parabolic shape, which are used to concentrate signals in a specific direction, and therefore often used in satellite communications and high-power wireless networks. Also, patch antennas, which are thin and flat, can be mounted on flat surfaces, and are common in smartphones and Wi-Fi devices. Finally, array antennas, which consist of a series of radiating elements arranged in a grid, offering high gain performance and directionality, often used in radar applications and high-speed wireless networks. These are just some of the most common types of antennas, but in general there is a wide range of designs and configurations that can be implemented, each designed to meet the specific needs of communication systems. Gain is a peculiar propriety of antennas, which represents the directional property of an antenna and can be expressed as the ability of the antenna to concentrate energy in a radius when transmitting, or when receiving as the ability to efficiently obtain the signal. The formula was discussed in section 2.1, and as can be seen from the latter, the higher G the more directional the transmitted signal would be.The antenna pattern is a mathematical model that describes the three dimensions spatial distribution of the electromagnetic waves emitted or received by an antenna. The pattern depends on the geometry and configuration of the antenna, as well as the characteristics of the surrounding terrain or environment in which the satellite operates.

So if the field points are positioned on a sphere, the direction to a field point is connected to the polar angles θ and ϕ by the relation:

$$\hat{r} = \hat{x}\sin\theta\cos\phi + \hat{y}\sin\theta\sin\phi + \hat{z}\cos\theta$$

A graphical description is shown in Figure 3.5.

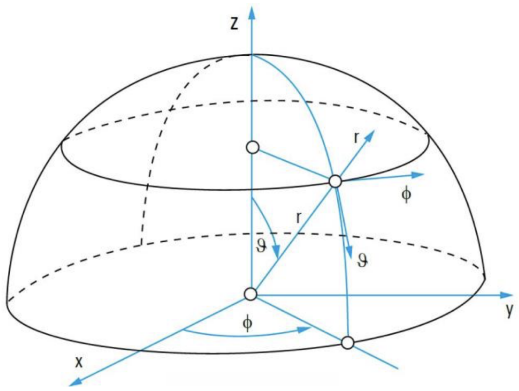

Figure 3.5: Polar coordinates in a spherical pattern [21]

Reports are supplied by the ESA mission studies, which provided details of the configuration of the electromagnetic signal emitted by the apparatus via a *.GRD* file. The GRD format is used to store field values in a rectangular grid, generated by objects of the Spherical Field Grid classes.
The elevation angle (θ), measures the height of a point relative to a horizontal reference plane. The azimuth angle (ϕ), measures the horizontal rotation of a point with respect to a reference plane, which in our case is the vertical plane containing the satellite's velocity vector. The procedure for fitting the gain data into our DEM, characterized by a matrix form, starts by calculating the square modulus of the antenna pattern, thus obtaining a two-dimensional gain model.
From this we further extract two variables, 'u' and 'v', which represent the azimuth and elevation values of the scene, and then go on to construct the grid points and proceed by calculating this two same parameters along the direction of the observation point relative to the center of the antenna,using two rotation matrices.

The last step was to create the interpolation between the general model parameters and the same ones projected along the scene, thus obtaining the antenna gain value in each pixel of the digital elevation model. Results are shown in Figure 3.6.

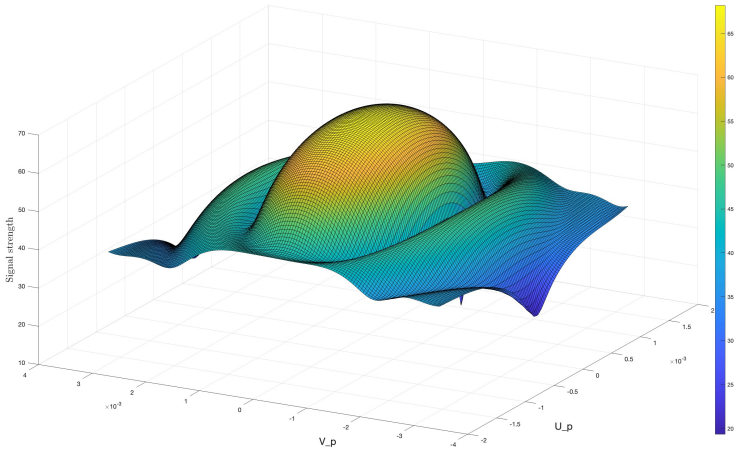

(a) 3D Pattern

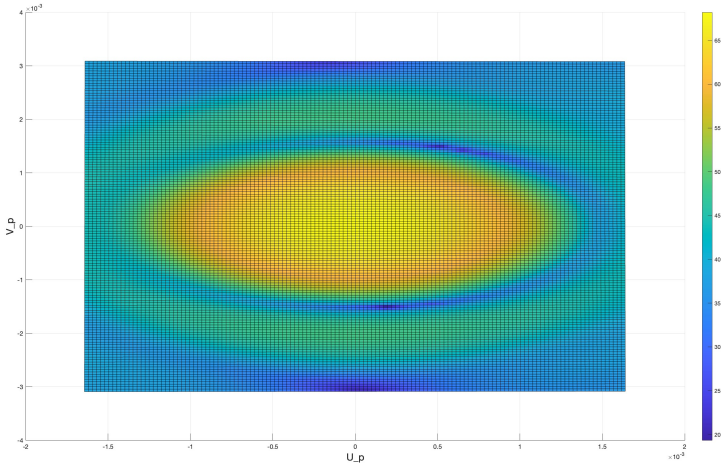

(b) 2D Pattern

Figure 3.6: Representation of the signal pattern of the antenna used in the WIVERN mission.

3.1.5 Shaded Areas

This MATLAB script is designed to evaluate the visibility of points on the earth's surface relative to a satellite. First, the code takes as input part of the heights contained in the DEM file, saved in a raster type form, the position of the satellite in space in a Cartesian reference system. As the study was implemented using data from the Piedmont orography, a critical height has been set, with a value of 5000 meters, because there are no mountains above this value in Europe Then a Boolean matrix is initialized to keep track of the visibility status of each pixel in the grid from the satellite position. The code performs an iteration on the grid defined by the coordinates in the plane x-y, representing the earth's surface. For each point on the grid, a vector, which represents the line connecting, is calculated which by subtracting the coordinates of the satellite from those of the specific points on the grid. Therefore this vector represents the direction from the satellite to the given point.

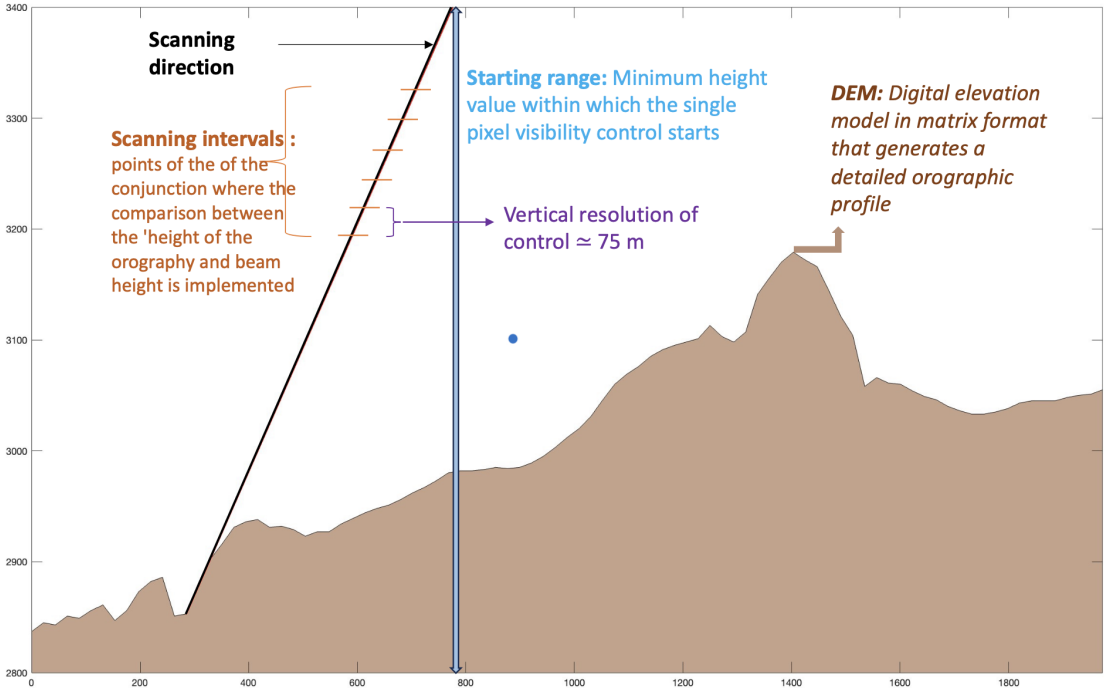

Figure 3.7: Mechanism of operation of the visibility algorithm

Next, the code performs an iteration along this direction. The iteration is performed from a certain point of this vector,which is called startRange and it's calculated with trigonometric laws starting from the defined critical height, to the position of the questioned point,through scan intervals of 75 m. During this iteration, the code evaluates the visibility of the point with respect to the satellite

and the terrain below.
For each intermediate position along the direction, the code calculates the coordinates of the conjunction line. These coordinates are obtained by interpolating the path between the satellite position and the position of the point on the grid. Next, the height of the terrain is interpolated using the interp2 function,so in every point of the grid we have a defined height.

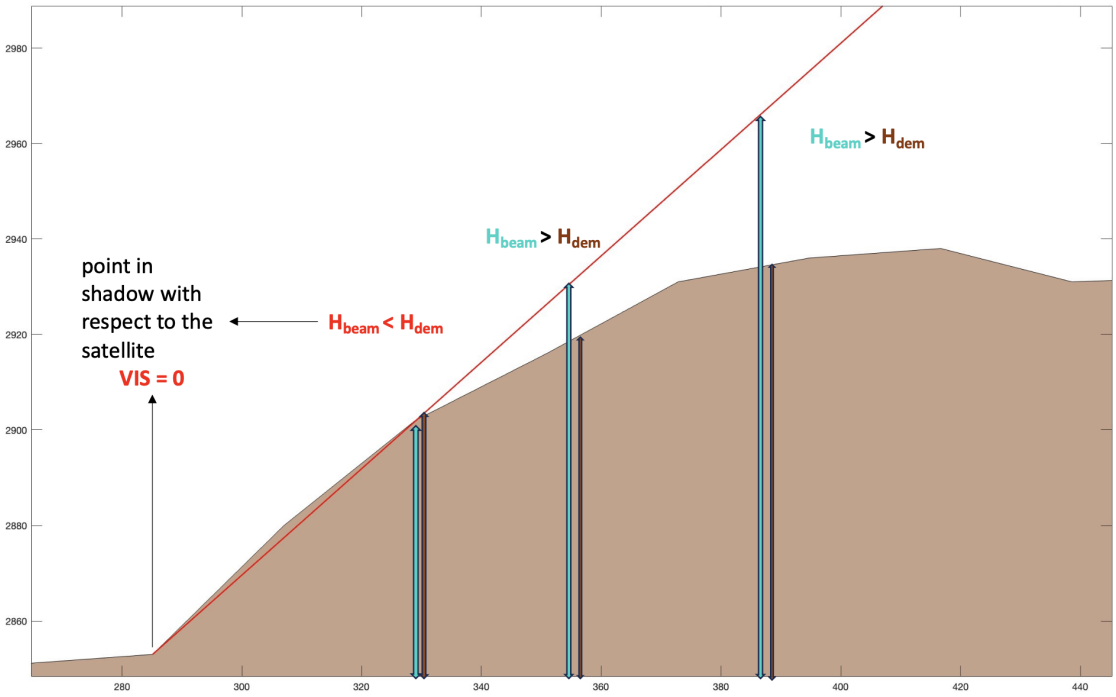

Figure 3.8: Covered line of sight

The script verifies if the z-coordinate of the conjunction is greater than that of the DEM. If so, the check continues until it reaches the x-y coordinate of the target point. If not, the visibility status is set to false, and the iteration is halted. This process iterates for each point on the grid. The resulting visibility status of each point is stored in the "i" matrix. Finally, the Boolean "isPointVisible" matrix is converted into a numeric matrix, indicating the visibility of points on the Earth's surface relative to the satellite using 0 and 1 flags.

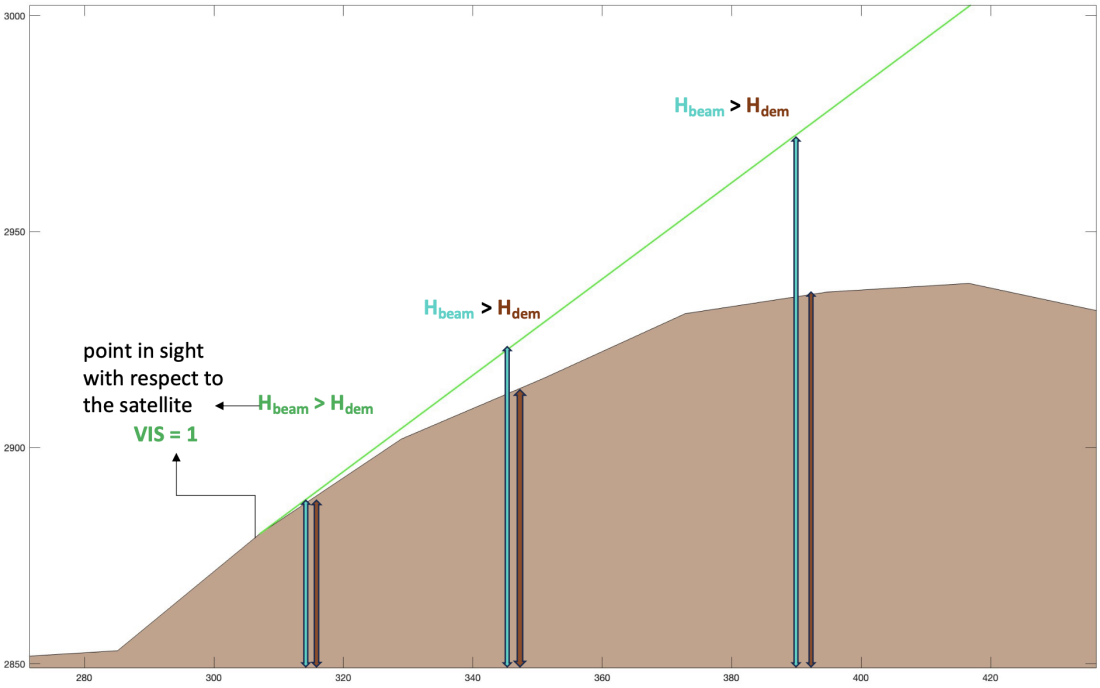

Figure 3.9: Clear line of sight

3.1.6 Terrain Characterization Model and RCS

As mentioned at the beginning of this section, in addition to elevation modeling data, to study how orography affects clutter, it is necessary to consider the different RCSs of the soils that make up the territory. This requires a detailed model of the types of soils in the Piedmont/Valdaostan area.

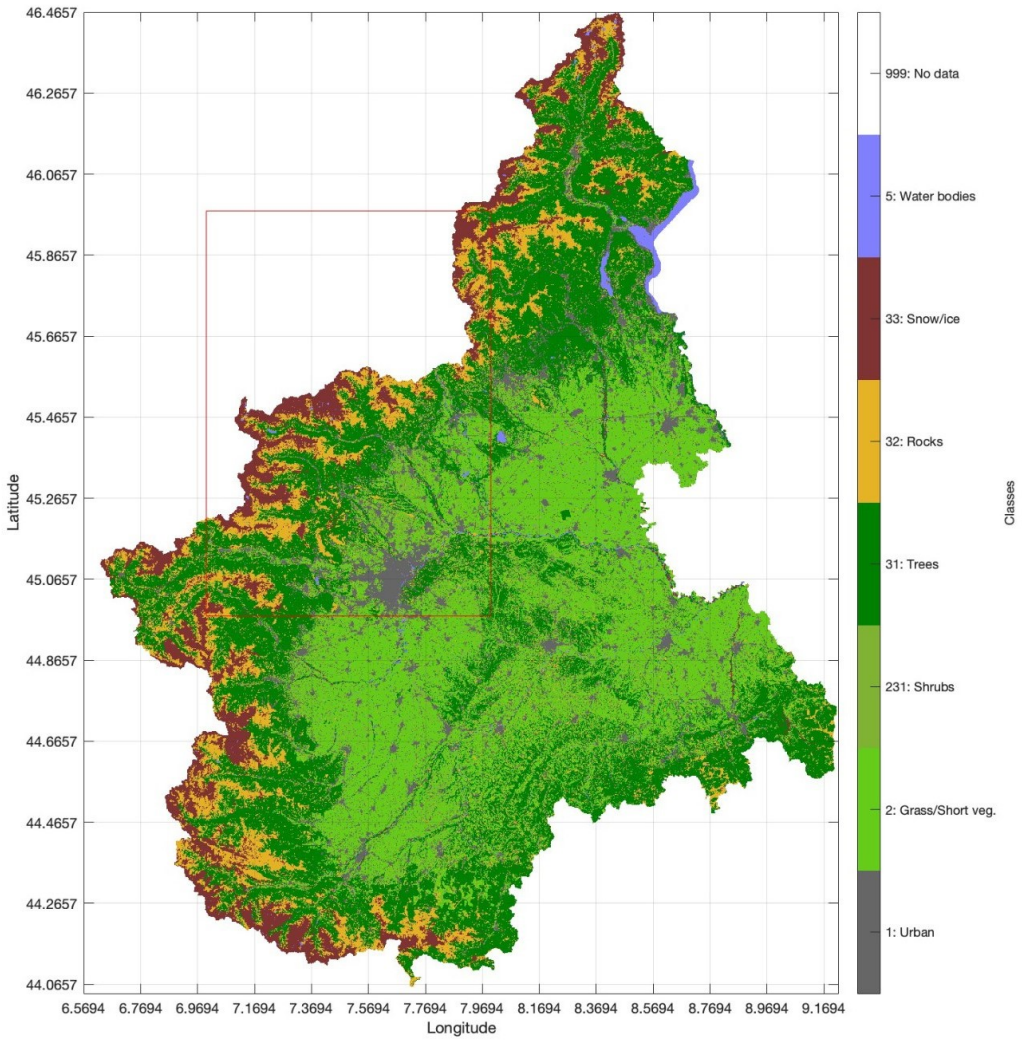

Figure 3.10: Terrain Characterization of the Piedmont.The red rectangle represent the latitude and longitude limits of the DEM

Stefano Campus, a member of the territorial agency GEOPIEMONTE, kindly provided this model, which transformed the original terrain data in vector format for the Piedmont region into a raster format characterized by an excellent resolution of about 20 m. The surface characterization involved many terrain categories for which data were unavailable in the look-up tables created earlier; thus, it was necessary to adapt the information to the nine categories for which σ_0 data were found.
For consistency with the categories in the GEOPIEMONT database, the categories short vegetation and grasses, such as dry snow and wet snow, and again urban and road, have been merged, resulting in only five macro-categories. A water body category derived from a function constructed from statistical data was added to these.
The raster data, as was the case with the DEM, was stored in a file.*tiff*. Then, similarly to what was done before, we went to extract the Geo-referenced information from the file and went to represent it (see figure: Figure 3.10.)
The terrain data covers the entire region, but for our study, only the area within the red rectangle in the image is required. Therefore, we limited the acquisition of file data to that specific area. Furthermore, due to higher resolution, especially along the latitudinal direction where the Digital Elevation Model has a pixel meshing of approximately 32 meters, we needed to interpolate the data within the grid generated by the DEM. This ensures consistency with the format used by other data packages, facilitating integration with the rest of the code. The result is a matrix containing integers, representing different land classes within Piedmont, preserving information about the type of land. This data is handled by an interpolation function designed to interpolate the radar cross-section based on factors such as the angle of incidence, polarization of the electromagnetic wave, and surface class. The radar back-scattering cross-section measures the energy reflected from a surface relative to the incident radar pulse. The polarization of the radar wave can be "vv" (vertical-vertical) or "hh" (horizontal-horizontal), indicating the polarization of the incident and reflected waves, respectively. The function begins by validating both the polarization and surface class provided. If the surface class is not valid, the value 999 is assigned, indicating "no data".
Next, based on the specified surface class, the function takes the incidence angles of each pixel of the scene, calculated in a previous section of the code, along with the corresponding radar cross-section values for the specified polarization, as input. These values are obtained from lookup tables constructed based on the study described in the Terrain types section. Finally, the function linearly interpolates the radar cross-section values based on the specified incidence angle, returning the interpolated value. If the specified incidence angle is outside the range of known angles, the function uses extrapolation to estimate the corresponding value.
An example of a visualization of the final result can be seen in Fig. 3.11.

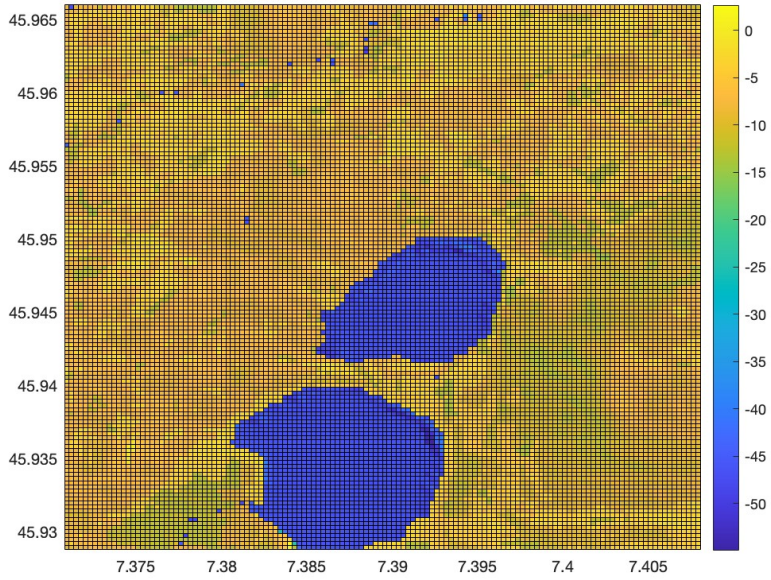

Figure 3.11: Avigliana's lakes in a RCS visualization

It is easily visible how lakes, and in general water surfaces have a much lower degree of reflection than all other materials which, remembering the image in Figure 2.4, present a radar cross section value that has a similar value for the different classes.The scene in question then has an elevation value characterized by a very small standard deviation of the datum, ergo the angle of incidence of the rays will be more or less constant,this justifies the fact that the areas outside the water body all present a very similar RCS value.

Chapter 4

Results and Analysis

In this chapter the full implementation of the radar clutter simulator is described. The simulator is exploited to produce profiles of the reflected power and of the reflectivity weighted Doppler velocity for few case studies where the radar footprint is moved in a mountainous region presenting both variability in the orography and of the radar backscattering cross section. A simulation of an antenna rotation scan with the footprint moving 125 meter from pulse to pulse with the corresponsing time series of reflectivity and Doppler profiles is presented as well.

Each part of the code, developed and validated in the context of the implemented research methodologies, was carefully integrated into a single computational framework, allowing for a comprehensive and detailed evaluation of the results obtained.
The analysis was carried out either by going to study a single scene ,of which the reflectivity and doppler curves were obtained,or by going to additionally implement the motion of the satellite when it rotates around its axis, thus making the antenna move and obtaining a series of different scenes,at a distance related to the pulsation of the emitted radar signal, so every 125 meters approximately.

4.1 Computation of reflectivity and Doppler profiles

The provided code implements a numerical integration using the method of trapezoids to calculate the integral of the two quantities of interest, which include contributions calculated in the previous section.

The method of trapezoids is an approximation technique used to calculate the integral of a function over a defined interval. Essentially, the method divides the integration interval into segments of uniform length and approximates the area under the curve of the function in each segment with a trapezoid.

Once the areas of the various trapezoids in each segment have been calculated, these areas are added together to obtain an approximation of the entire integral. "This method provides an effective approach to approximating the area under the function curve, which integrates well with the concept of sampling, related to pulsed radar operation.

Code

The code performs numerical integration using this integration method to calculate two fundamental quantities:the power density received by the radar, and the reflectivity weighted Doppler velocity(RWDV). These quantities are crucial to understanding the radar response and the characteristics of the observed surface.

The main loop runs over a set of values defined in the delta range. This vector contains the center points of the sampling bands along the pulsed radar trajectory.

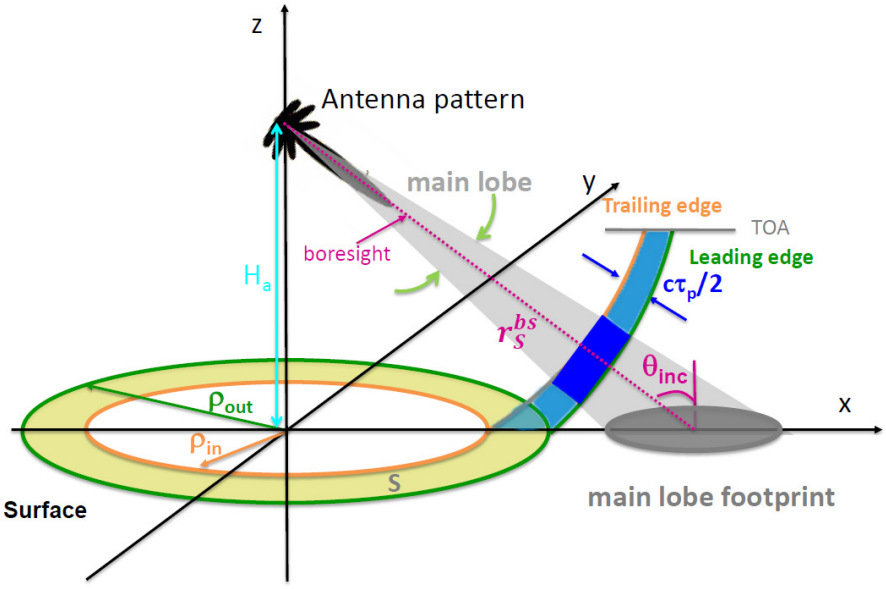

Figure 4.1: Display of pulsed radar operation

Here, we make the assumption that the radar's transmitted pulse takes on a top hat shape, lasting for a duration of τ, and is emitted in accordance with an antenna pattern characterized by a primary lobe (illustrated by the light grey shaded cone) and various sidelobes (depicted as black envelopes). The power received at any given time t (and the corresponding range r = $c\tau/2$, where c represents the speed of light) stems from the contributions of targets situated within spheres centered around the radar and formed by the propagation of the pulse's trailing and leading

edges. These are represented in Figure 2 by orange and green lines, respectively. When dealing with a flat surface, these targets form a surface annular strip of terrain, as outlined in Battaglia et al.(2017)[14]. However, we need to specify that in the context of complex terrain, such regions, referred to here as S, become significantly more intricate and are influenced by factors such as illumination geometry and topography.
All the data that are part of the same window then go on to contribute to the value of a single element in each of the two vectors by the summation operation. Subsequently of these indices, only specific ones are selected based on the value of the rescaled gain by applying a 30 dB thresholding. This selection is critical to isolating regions of interest on the observed surface, and the choice of threshold value will be justified in the Sect. 4.1.1. From the computational point of view, the formula described in the section 2.1 , the power received by the radar from the surface at range r, P_r, assuming that the antenna gain is identical for transmission and reception, is given by an integration performed over the illuminated area, S, [22, 23]:

$$\begin{aligned} P_r(r) &= \underbrace{\left[P_t \frac{\lambda^2}{(4\pi)^3} G_0^2\right]}_{C_S} \int_{\mathrm{S}} \frac{\sigma_0(\psi)\ G_n^2\ \left|u(t-2r/c)\right|^2}{r^4}\ dS \\ &\approx C_S \sum_{i,j} \frac{\sigma_0(\psi_{ij})\ G_n^2(\mathbf{u}_{ij}^{LoS})\ \left|u(t-2r_{ij}/c)\right|^2}{r_{ij}^4} dS_{ij} \end{aligned} \tag{4.1}$$

where P_t is the transmitted power, λ is the wavelength of radar, $G = G_0 G_n$ is the antenna gain (G_0 being the maximum gain at antenna boresight), $u(t)$ is the complex voltage envelope of the transmitted pulse (for a top hat shape $|u(t)| = 1$ for $0 < t < \tau_p$), ψ is the local incidence angle that can be computed as $\psi = acos(\mathbf{u}_{ij}^{LoS} \cdot \mathbf{u}_{ij}^{n})$ where $\mathbf{u}_{ij}^{n}$ is the normal to the infinitesimal surface. The integral (summation) is extended only to those pixels that are visible from the radar (see Sect. subsection 3.1.5).Note that a radar constant C_S relevant for a surface target has been introduced.
In radar meteorology for meteorological distributed targets the radar reflectivity is defined as:

$$P_r(r) = C_M \frac{Z_e}{r^2} \qquad \text{where } C_M \equiv \frac{\pi^2}{2^6} \frac{P_t\, G_0^2 \Omega_{2A}}{\lambda^2} \frac{c\tau_p}{2} |K_w|^2 = C_S \frac{\pi^5 \Omega_{2A}}{\lambda^4 |K_w|^2} \frac{c\tau_p}{2} \tag{4.2}$$

with K_w being the dielectric factor of water at 3 mm-wavelengths (assumed equal to 0.78), $\Omega_{2A} \equiv \int G_n^2 d\Omega$ (which for a Gaussian beam is approximately equal to $\frac{\theta_{3dB}\phi_{3dB}}{8\log(2)}$) and C_S is another radar constant, previously defined in Eq. (4.1). Eq. 4.2 allows to convert P_r to Z_e for any given range.

The Doppler velocity at range r is computed similarly to Eq. 4.3

$$v_D(r) = \frac{C_S}{P_r(r)} \sum_{i,j} \frac{v_{SC}(ij)\sigma_0(\psi_{ij})\ G_n^2(\mathbf{u}_{ij}^{LoS})\ \ |u(t - 2r_{ij}/c)|^2}{r_{ij}^4}\, dS_{ij} \tag{4.3}$$

where $v_{SC}(ij) = \mathbf{u}_{ij} \cdot \mathbf{v}_{SC}$ is the projection of the satellite velocity along the line of sight described in subsection 3.1.3. The reason we refer to this quantity as reflectivity weighted Doppler velocity can be understood just from the Equation 4.3, the whole calculation being related to the reflectivity of the surface.

4.1.1 Sensitivity Analysis

A sensitivity analysis is essential to understand how large the scene should be in terms of antenna gain in order to achieve optimal convergence of the integrals.

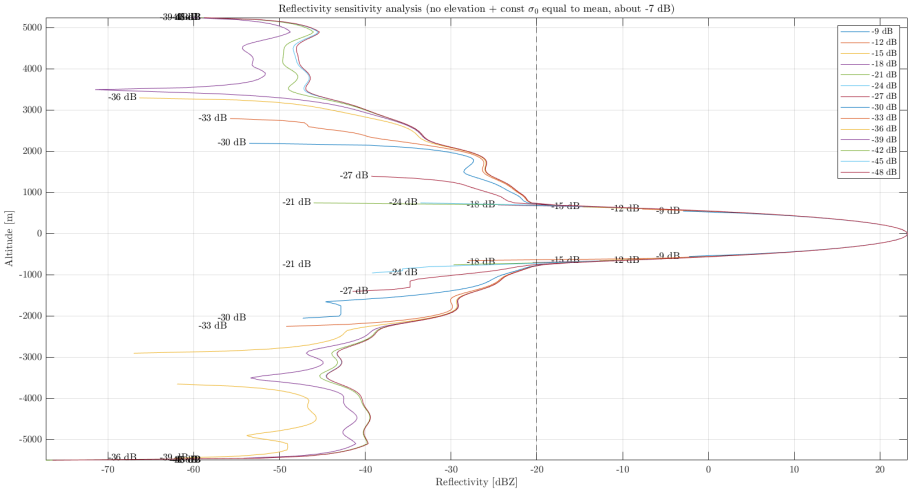

Figure 4.2: Power density as a function of the gain level threshold. The dotted line represents the typical average value of background noise.

In this context, the main objective is to determine the optimal size of the scene, i.e., the area over which the analysis is performed, in relation to the characteristics of the antenna, particularly its gain onto the scene. By lowering the limit of minimum value of Gain from that at boresight, more points in the iteration are going to be considered for reflected power,which will have an obviously lower contribution since it is weighted by the gain at that point but which can improve the sensitivity of the system.
However, it is important to balance this increase in sensitivity with other factors, the most important of which is background noise. Excessive sensitivity can lead to

too high an increase in the signal-to-noise factor and receiver saturation problems, compromising the overall effectiveness of the system.
In order to conduct an accurate sensitivity analysis, it was necessary to evaluate various scenarios graphically, going to plot the power density obtained by taking into account more and more points based on the lower gain value of the antenna, rescaled by the value of that variable at boresight, and observing how it affects the convergence of the integral and the accuracy of the results obtained. It was then possible to determine the optimum point at which the scene size and antenna gain maximize the useful information extracted from the signal, while ensuring efficient and reliable operation of the radar system. The limiting value derived is precisely -30 dB, as the scene becomes large enough for the calculation to converge, reaching a size of about 7 square kilometers, but at the same time small enough that the signal strength is not too faint compared to the background noise. It should be noted that the effect of noise was not actually considered in the analysis, but was nevertheless taken into account here in order to ensure that the results were realistic.

4.1.2 Case studies

The discussion will first take place by showing and thoroughly analyzing the single-footprint results then we will proceed with the analysis of the multiple footprint results, where numerous successive footprints separated by 125 m will be considered.

Single-footprint

The chosen area is represented in Figure 4.3 and Figure 4.4, and it is possible to visualize its position in the DEM in 4.11.

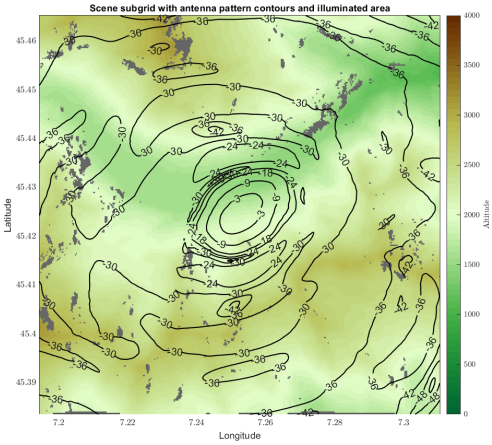

Figure 4.3: Scene with antenna pattern contours and illuminated area (x-axis: Longitude, y-axis: Latitude).

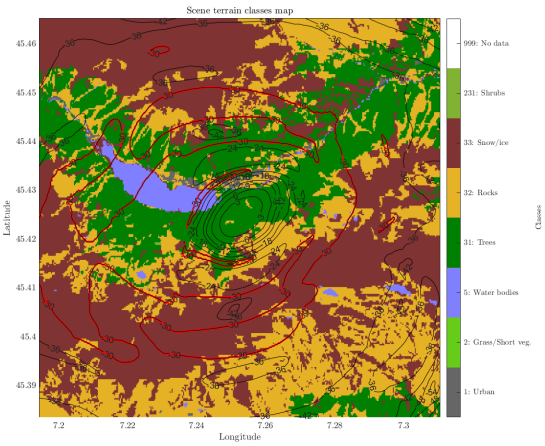

Figure 4.4: Scene Terrain classes map (x-axis: Longitude, y-axis: Latitude)

The chosen area, located at the foot of the Gran Paradiso mountain, is of particular interest since it combines well both the effect of a very pronounced orography and the presence of different types of terrain that includes a lake, very useful to see the abrupt lowering of RCS of terrain. The quantities we are going to plot are just the Z_e and v_D defined in Eq. 4.2-4.3. Starting from the reflectivity, in Figure 4.5 the function for both the real and simplified case is represented. In the first condition, the combined effect of the variation of both the altitude variation and of the normalized radar cross section are accounted for.
The second case is the one is called flat ground, since the elevation values of the pixels in the scene have been set equal to the average value in the area, with an RCS value equal to the average in the area and therefore constant as well.

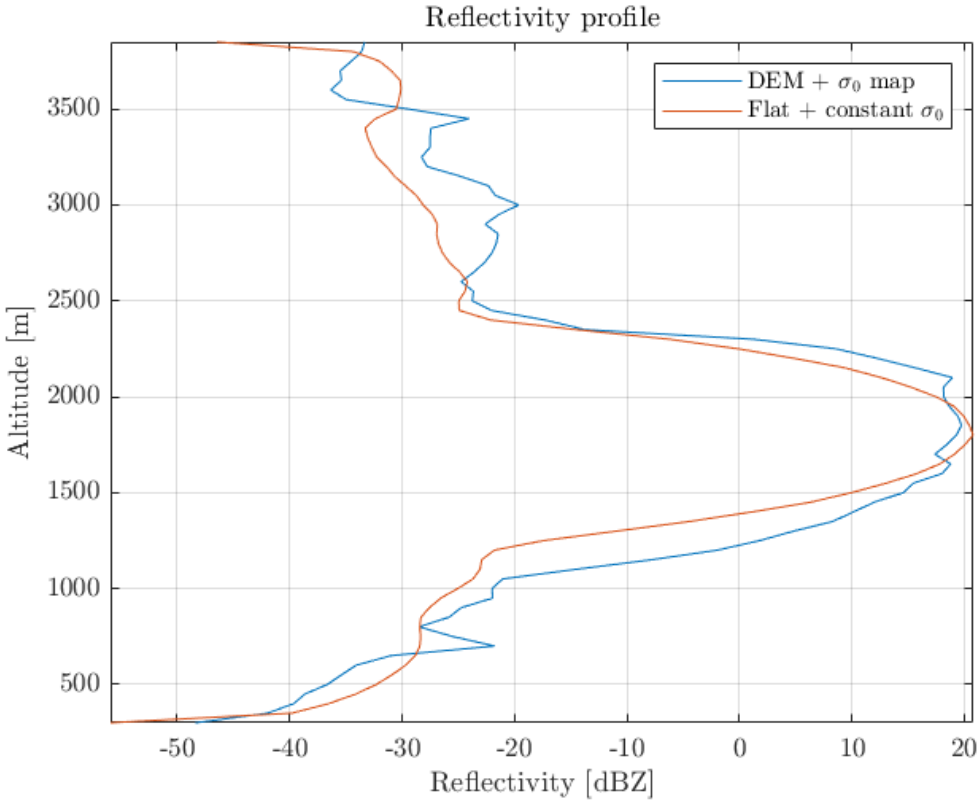

Figure 4.5: Comparison between the clutter reflectivity profile in a real and ideal scenario.

The combined effect of the gradients of these quantities within the area leads to substantial differentiation in the shape and amplitude that the feature takes.
In particular, the presence of a complex orographic profile leads to the breaking of the regular shape of the case in flat earth. The various peaks and valleys of the

environment make the profile of the ISO-range areas of which the satellite detects the reflected power very anomalous and peculiar, joined to the presence of shaded points that will no longer contribute to the detected value, thus creating areas, along the scan height diagrammed on the ordinates of the Figure 4.5, favored from the point of view of signal irradiation at the expense of others that will contribute less, thus creating fluctuations in reflectivity, with local peaks and troughs in the received signal, which go on to generate a different form of the function for each type of surface observed.
This effect is more pronounced the larger the standard deviation of elevation in the analysed scene.

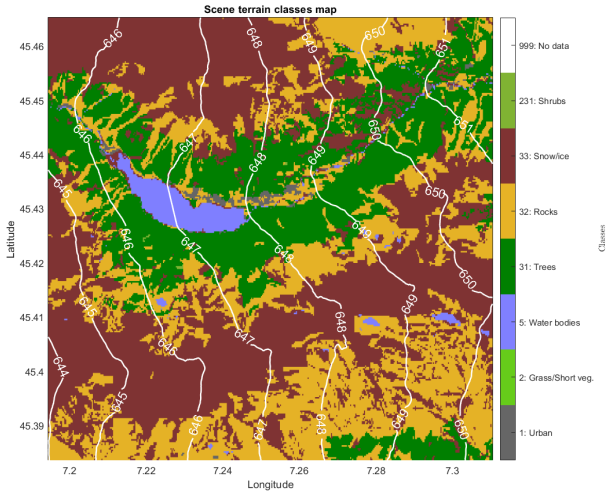

Figure 4.6: ISO-range zones over the classes map of the analyzed region

The presence of a real trend in the Radar Cross Section (RCS) affects the signal amplitude, leading to a modulation of the function. Typically, due to the negative trend of RCS with respect to the angle of incidence, this modulation tends to decrease the reflectivity values. Since backs-scattering cross section is multiplied by the contributions of individual pixels in the calculation of reflected power, this trend results in lower overall values.
In our simulation, we characterized the simplified case by using the average RCS of the scene. This approach ensured that the values did not undergo excessive rescaling, and any general lowering was compensated by contributions from other integral elements.
As for the reflectivity-weighted Doppler velocity, the direction of observation relative to the satellite movement comes into play as well. In fact, the orientation of the ISO-range lines with respect to the ISO-Doppler lines becomes fundamental,and

two extreme cases can be delimited: assuming that the satellite is moving along the north-south orientation, when the position versor of boresight is pointing at the furthest western or eastern point relative to the scene, it's a scenario referred to as the *Side* configuration. Instead, when the versor of boresight is aligned directly with the motion of the spacecraft, so to north or south, the case is denoted as the *Forward* configuration. In Figure 4.7 are shown two simplified cases.

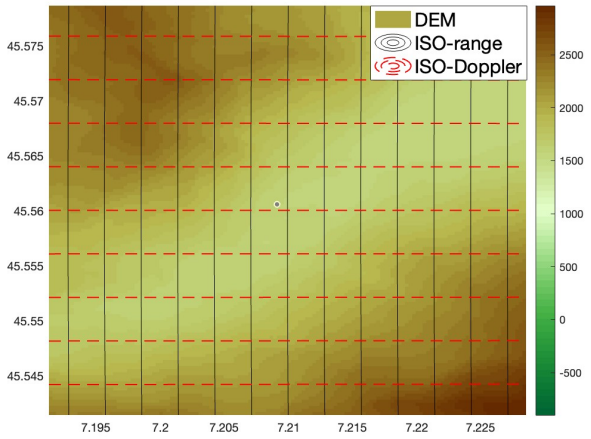

(a) ISO-levels zones in side view.

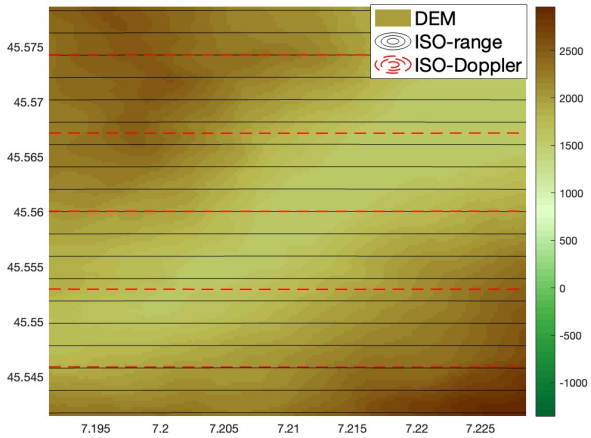

(b) ISO-levels zones in forward view.

Figure 4.7: ISO-r and ISO-d calculated in the case of flat earth and represented on the DEM of the area under analysis.

In the first case, on the left side of Figure 4.7, we are in the side configuration. Here, the ISO-level curves are perpendicular to each other. Therefore, values will all fluctuate around 0 m/s.
In the second case, on the right side of Figure 4.7, we are in the forward configuration. Here, being the curves parallel one to another, the calculated velocity will symmetrically go from the minimum to the maximum value at the same time as the range grows.
This can be seen in Figure 4.8.

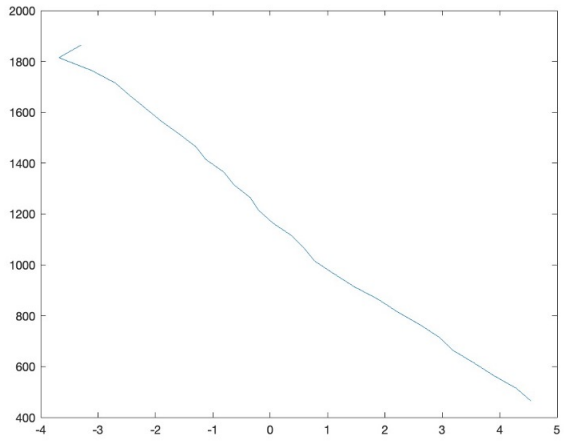

Figure 4.8: Example of a general RWDV in a forward configuration

Let us analyze the case in side configuration since the real surface effect causes more significant imbalances being the theoretical RWDV always around 0 m/s.

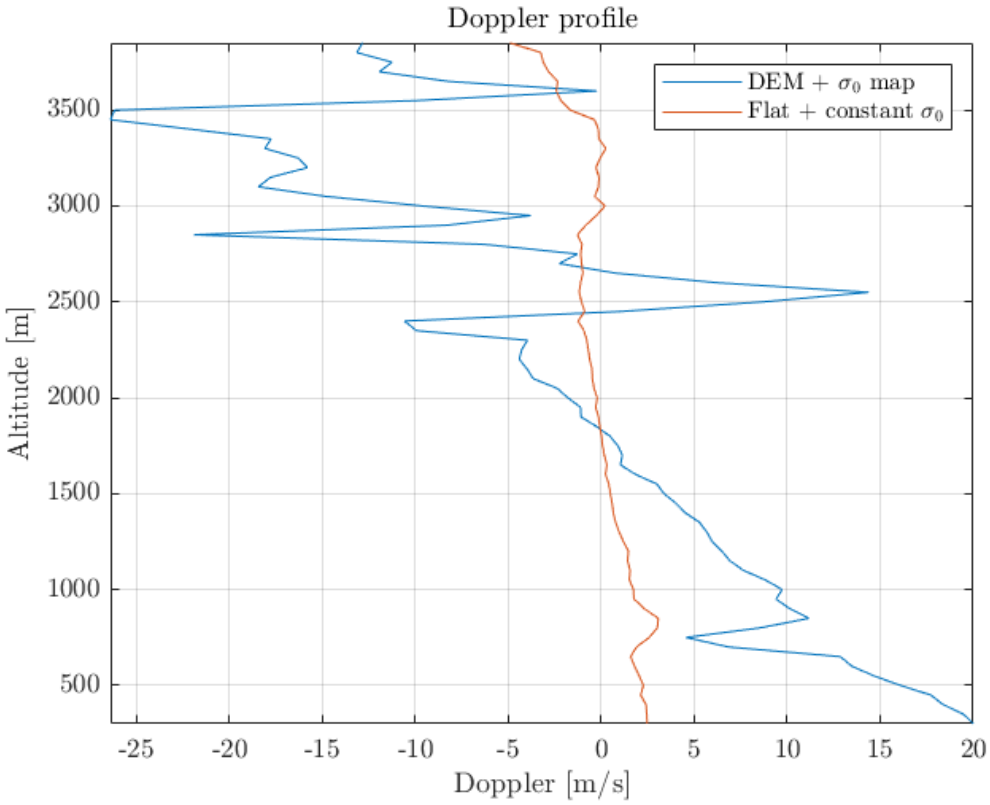

Figure 4.9: Comparison of RWDV trend as a function of distance from the ground between a real surface, in blue, and an ideal surface, in red.

From Figure 3.9 it is easily noticeable how the ideal trend is extremely perturbed by the presence of elevation gradients and by the inhomogeneity of the radar cross section within the integration area. In particular, the latter is usually referred to as nonuniform beam filling. This concept refers to the nonuniform spatial distribution of the backscattered energy, which affects unevenly the reflectivity-weighted Doppler velocity estimate. In the context of a Doppler radar, RWDV combines the radial velocity information of a target with the reflectivity of the target, which in our case is the surface. However, if the area of an illuminated target is not uniformly invested by the radar beam, and/or the reflection properties of the target are spatially variable, a nonuniform distribution of the signal energy extremely affects the reflectivity-weighted Doppler velocity estimate.
Since the received radar signal is neither uniformly distributed over its surface, nor reflected equally in all areas, the parts of the target with a higher RCS value will

receive a greater weight in the Doppler velocity estimate, depending on the type of terrain encountered as well as the incidence with which the beam strikes the surface. Consequently, if the target is moving, its reflectivity-weighted Doppler velocity estimate will be completely different from the ideal case at a flat surface and constant RCS, as can be seen in Figure 4.9.

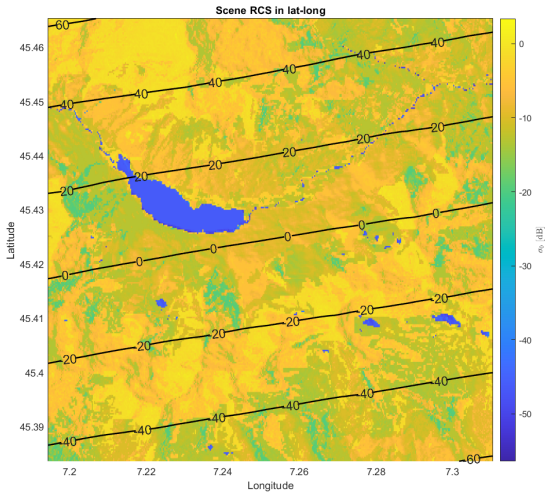

Figure 4.10: Graphic representation of ISO-Doppler zones on the map characterizing the 'cross section radar pattern

By analyzing Figure 4.10 that plots the ISO-Doppler on the RCS map, it can be seen that the areas marked by a Doppler velocity less than zero (the areas below the center line) have on average a higher back scattering cross-section, due mainly to the absence of a water surface of noticeable size. In fact, water is characterized by an extremely low reflectivity value, even relative to the other soil types as can be seen from the σ_0 values (colorbar on the right hand side of the panel).

50 km long scan

In this section of the analysis the serial data acquisition by the satellite will be discussed, going to iterate the code along a ground track of about 50 km, thus taking into account the data of 400 footprints. It should be specified that the ground track of the satellite is constructed from the rotational motion of the antenna around its vertical axis, without considering the motion of the satellite in its orbit. This simplification is not particularly relevant from the point of view of simulation accuracy since, considering the conditions under which the satellite operates, a time interval of about one fifth of a second is being simulated.

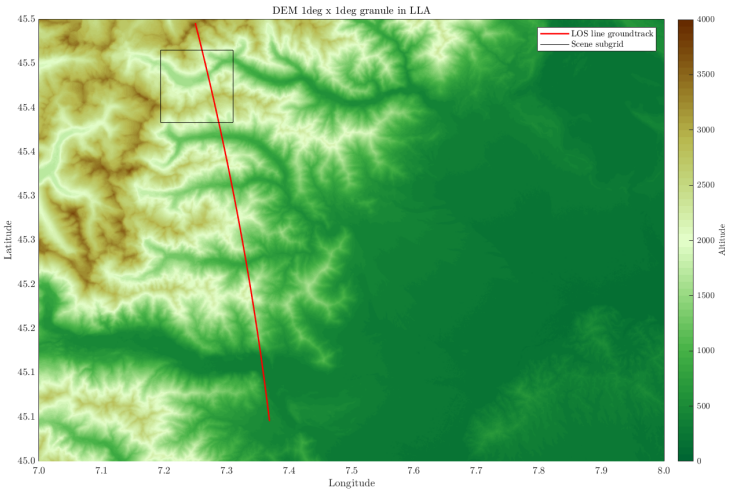

Figure 4.11: Example of Wivern's antenna scanning geometry in quasi SIDE configuration

Figure 4.11 represents just the trace on the surface of the various boresights along the arc of circumference drawn by the rotation of the antenna, moving from the western alpine zone, thus characterized by a very pronounced orography, to a more flat one. The black box represents the single-footprint simulated and analyzed in section 4.1.2. As is evident we are in configuration *Side*.

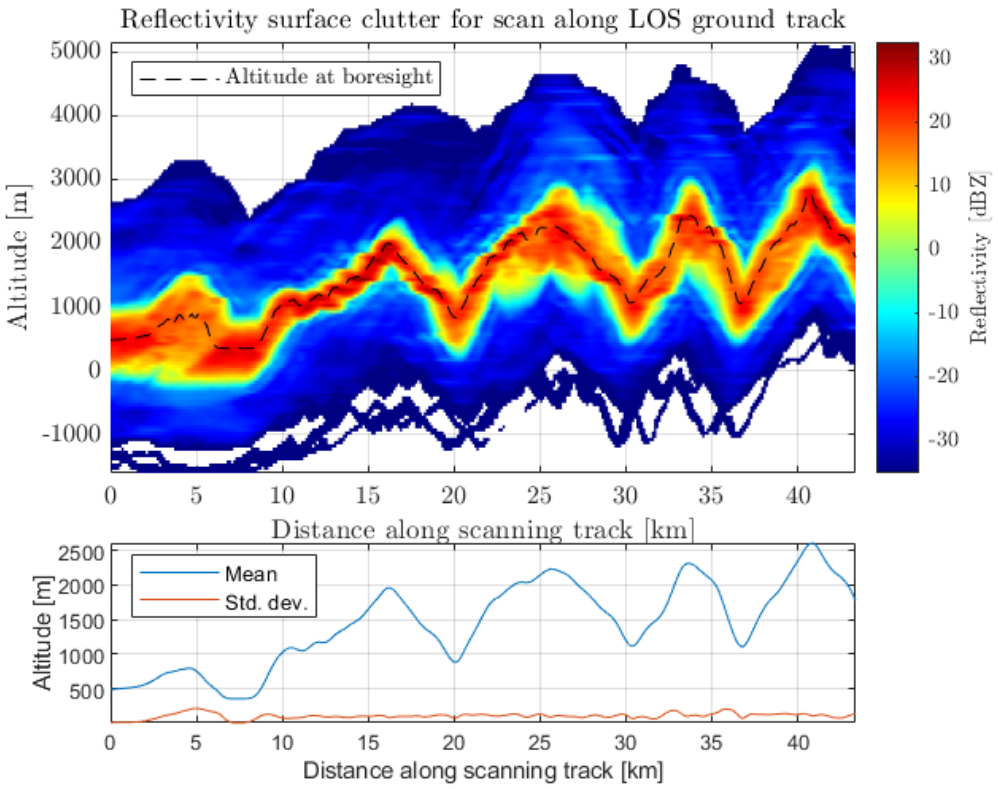

Figure 4.12: Multiple footprints simulation of Reflectivity

The result obtained from the simulation for the reflectivity profile is shown in Figure 4.13. In addition, the information about the mean value of the elevation and of its standard deviations are presented in the lower panel. The dashed black line in the upper panel represents the mean altitude of the surface.
This simulation provides crucial information on the reflectivity generated by clutter, which is considered a disturbance in the Wivern mission as it is aimed at observing hydrometeors. However, these data are also relevant for any other Earth observation mission, as distinguishing signals from noise is a very complex and important issue. In addition, the graph makes it possible to extrapolate information about the distance from the surface at which the phenomenon of interest can be analyzed. This can be essential for the analysis of important problems such as Orographic Enhancement, like explained in section 1.1.

If we consider data on the reflectivity in the W band typical of rain or snow under different conditions, as obtained in the work of [24], we can infer how large the signal to clutter could be as a function of distance from the surface.

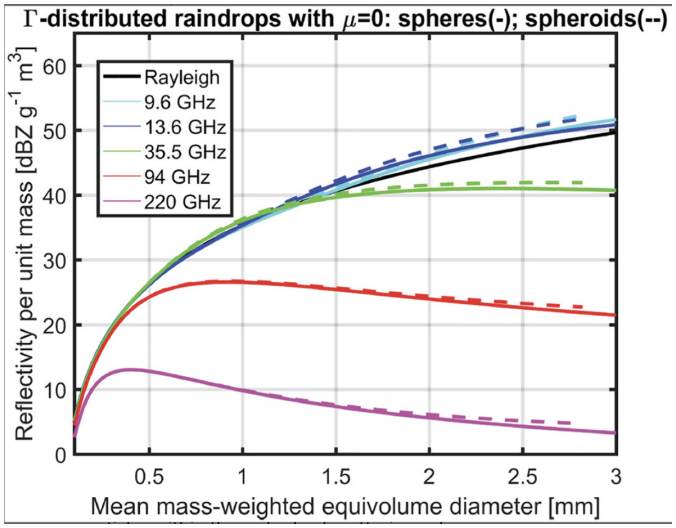

Figure 4.13: Radar reflectivity coefficients for different frequencies for an exponential population of raindrops with different mean mass-weighted equivolume diameters for a liquid water content of 1g/m^3.

Figure 4.13 describes a scenario of non-Rayleigh scattering, where the size of raindrops becomes comparable to or larger than the wavelength, and the backscattering power exhibits a pattern of oscillation, characterized by consecutive maxima and minima as the size increases.

Conversely, Figure 4.14, for the case of ice crystals, shows the observed range of variability for a given size underscores the inherent uncertainty in scattering properties due to ice microphysics. Notably, heavily rimed crystals are found to backscatter up to 10–15 dB more than fluffy aggregates with equivalent mass content, accentuating the diverse scattering behavior within ice crystal populations. In general, the reflectivity of rain is much higher than that of snow, although their values depend on the severity of the climatic event, which causes their physical properties to vary. Considering a very high intensity weather event, the rain will reach values of about 25-30 dBZ, while graupel will likely stop at 20 dBZ (considering heavily rimed crystals). It is interesting to analyze how far Wivern could detect such events without going against the blinding effect of clutter.

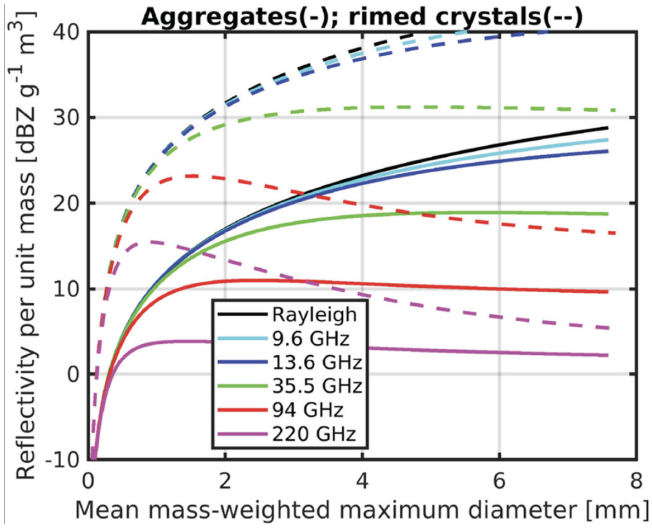

Figure 4.14: Radar reflectivity coefficients for different frequencies for an exponential population of ice crystals with different mean mass-weighted maximum diameters for an equivalent liquid water content of 1g/m3.Continuous lines and dashed lines correspond respectively to fluffy aggregates and heavily rimed crystals.

Choosing to implement the measurements in the forest of the "Collina Morenica di Rivoli", about the fifth km of the scan, since it is characterized by a very large high reflectivity zone around the boresight, this will result in a fairly substantial detection disturbance effect. Nevertheless in the event of a phenomenon like a cloudburst, characterized by an intense and sudden atmospheric precipitation, by comparing the data from the clutter simulation with the data from the 'analysis described in Figure 4.13 and Figure 4.14, looking at the maxima of the two functions, it emerges that would be possible to successfully detect the phenomenon up to a height that is substantially those of the surface, if the precipitation was composed of rain, or an height which is in the range of hundreds of meters, in the case of graupel.

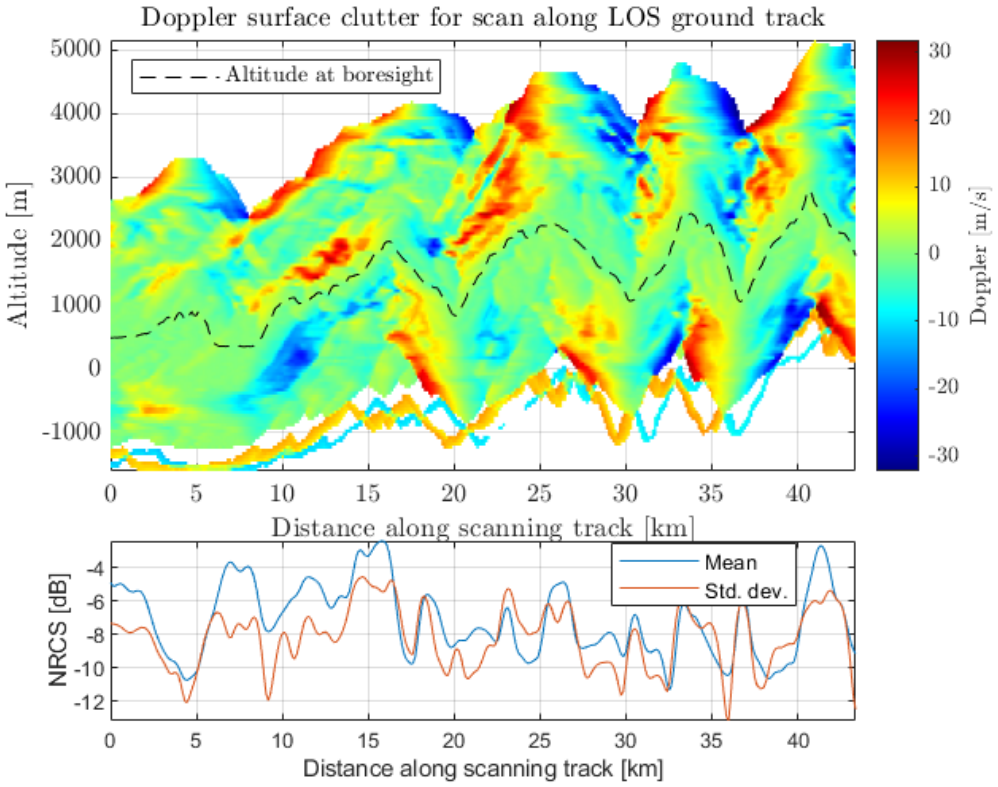

Figure 4.15: Multiple footprints simulation of reflectivity weighted Doppler velocity in SIDE configuration

Figure 4.15 depicts the result of the same type of simulation for RWDV. The decision was made to show the relationship between the weighted velocity around the boresight, the Radar Cross Section σ_0 of the scanned areas with its standard deviations, because it was observed that this parameter has the greatest impact on

this type of measurement, especially in relation to our objective. Upon reviewing the simulation results, it becomes evident that in the side configuration, where the results hover around 0 $\frac{m}{s}$, there are significant discrepancies due to the phenomenon of non-uniform beam filling caused by the complex RCS profile. These substantial inconsistencies make the implementation of RWDV-based calibration extremely complex, and thus it is inconvenient to apply it with this scan geometry.
For our analysis, it is more beneficial to focus on examining the Range Weighted Doppler Velocity (RWDV) in a forward configuration.

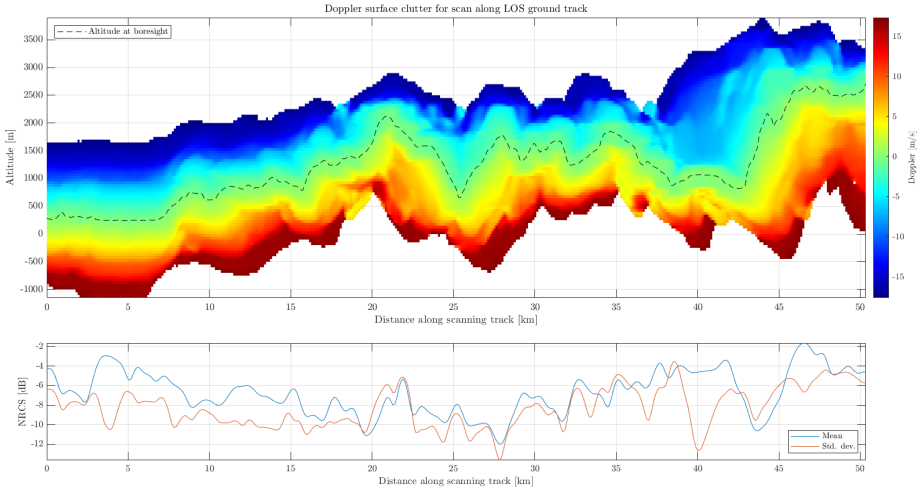

Figure 4.16: Multiple footprints simulation of reflectivity weighted Doppler velocity in FORWARD configuration

Despite the presence of a fairly complex RCS scene in this scenario, the ISO-range and ISO-Doppler zones are aligned to be nearly parallel, as was shown in Figure 4.7. This alignment results in the RWDV calculation yielding a decreasing straight line, transitioning gradually from negative to positive values (see Figure 4.8). Consequently, the effect of non-uniform beam filling, although present, is attenuated and carries less significance for our objectives as it is demonstrated in 4.16. In fact, notably around the boresight, the velocity consistently registers zero, providing a reliable reference point for implementing Doppler calibration.

Chapter 5

Conclusion

This study was conducted in order to go and analyze and propose a solution to two fundamental problems in meteorological radar, namely the problem of mispointing and the characterization of the signal-to-clutter ratio, which is, in particular, a critical problem in modern radars, because of the blind zone that it generates which is an obstacle to the aim to observe atmospheric phenomena (clouds and precipitation), as in the case of the WIVERN mission.
It is essential to have a prediction of clutter as faithful to reality as possible, taking into account the intricate effects developed by the presence of individual topography and surfaces with different degrees of σ_0. In addition, an accurate measurement of the surface Doppler velocity, could be exploited precisely as a reference point for implementing a calibration of the Doppler velocity products. Our work resulted in developing a simulator capable of calculating reflectivity for complex profiles and determining the value of RWDV in the analyzed scene. This achievement was made possible through several key steps on order to obtain all the components necessary for the integration of the radar equation, allowing us to construct all the necessary elements for the simulator.
As a result, we obtained a tool that enables precise calculation of reflectivity for each type of profile. Furthermore, this simulator utilizes the obtained data to derive the reflectivity-weighted Doppler velocity information. This aspect is particularly significant as it lays the foundation for further research into the potential use of this measurement to calibrate antenna pointing. It is important to remark that Doppler velocity is inherently linked to the direction of scanning relative to the direction of motion.
This study's implications could be significant in various fields, particularly in space-borne cloud and precipitation radar missions. The methodology's adaptable nature suggests that it could be applied to a wide range of missions in this domain. One example of possible use could be the upcoming ESA's EarthCARE (Cloud, Aerosol and Radiation Explorer) mission ([25]) , which will be launched in May

2024, and will work on advancing the understanding of the role that clouds and aerosols play in reflecting incident solar radiation into space and trapping infrared radiation emitted from Earth's surface. That mission will deploy a W-band radar system like WIVERN but with a nadir incidence. This implies that the clutter signal will be extremely relevant in the measurements because of the high RCS function at such angles.

There are caveats to be taken into account in order to go about improving such a simulator for which integration into the code will be useful, including also considering the orbital motion of the satellite and especially including a function that generates some background noise in the measurements. Although clutter was calculated meticulously, its measurement should also include an element of noise since this is intrinsic to the measurement itself. The receiver of the apparatus measures electrical voltages proportional to the return signal it receives. However, these are disturbed due to the temperature of the receiver itself during its operation, which for WIVERN generates a reflectivity equivalent noise of about -20 dBZ. Thus, in order to ensure a simulation as faithful as possible to reality, it will be necessary to implement it.

Moving forward, it would be valuable to explore the possibility of creating a database that considers how the Z_e and RWDV vary as a function of the standard deviations relative to the elevations and RCSs of the observed scenes. This will be possible by analyzing thousands of cases with different combinations of these two parameters to do an accurate statistical analysis evaluating how and to what extent the calculated profiles deviate from the values of ideal profiles. Such an objective would be beneficial, especially from the point of view of antenna calibration, since it would allow to selection of the surfaces of the Earth that would permit accurate calibration based on simple criteria related to the standard deviations of the elevations and of the RCSs.

Bibliography

[1] A. J. Illingworth et al. «WIVERN: A New Satellite Concept to Provide Global In-Cloud Winds, Precipitation, and Cloud Properties». In: *Bull. Amer. Met. Soc.* 99.8 (2018), pp. 1669–1687. DOI: 10.1175/BAMS-D-16-0047.1. eprint: https://doi.org/10.1175/BAMS-D-16-0047.1. URL: https://doi.org/10.1175/BAMS-D-16-0047.1 (cit. on pp. 1, 2).

[2] A. Battaglia, P. Martire, E. Caubet, L. Phalippou, F. Stesina, P. Kollias, and A. Illingworth. «End to end simulator for the WIVERN W-band Doppler conically scanning spaceborne radar». In: *Atm. Meas. Tech.* 2021 (2022), pp. 1–31. DOI: 10.5194/amt-2021-342. URL: https://amt.copernicus.org/preprints/amt-2021-342/ (cit. on pp. 1, 4).

[3] ESA WIVERN-RfA. *WIVERN Report for Assessment*. Tech. rep. available at https://eo4society.esa.int/event/earth-explorer-11-user-consultation-meeting/. ESA-EOPSM-WIVE-RP-4375, 2023 (cit. on p. 1).

[4] Ali Rizik, Alessandro Battaglia, Frederic Tridon, Filippo Emilio Scarsi, Anton Kötsche, Heike Kalesse-Los, Maximilian Maahn, and Anthony Illingworth. «Impact of Crosstalk on Reflectivity and Doppler Measurements for the WIVERN Polarization Diversity Doppler Radar». In: *IEEE Transactions on Geoscience and Remote Sensing* 61 (2023), pp. 1–14. DOI: 10.1109/TGRS.2023.3320287 (cit. on p. 1).

[5] A. Battaglia, F. E. Scarsi, K. Mroz, and A. Illingworth. «In-orbit cross-calibration of millimeter conically scanning spaceborne radars». In: *Atm. Meas. Tech.* 16.12 (2023), pp. 3283–3297. DOI: 10.5194/amt-16-3283-2023. URL: https://amt.copernicus.org/articles/16/3283/2023/ (cit. on p. 1).

[6] F. Tridon, A. Battaglia, A. Rizik, F. E. Scarsi, and A. Illingworth. «Filling the Gap of Wind Observations Inside Tropical Cyclones». In: *Earth and Space Science* 10.11 (2023). e2023EA003099 2023EA003099, e2023EA003099. DOI: https://doi.org/10.1029/2023EA003099. eprint: https://agupubs.onlinelibrary.wiley.com/doi/pdf/10.1029/2023EA003099. URL: https:

//agupubs.onlinelibrary.wiley.com/doi/abs/10.1029/2023EA003099 (cit. on pp. 1, 2).

[7] A. Battaglia, R. Dhillon, and A. Illingworth. «Doppler W-band polarization diversity space-borne radar simulator for wind studies». In: *Atm. Meas. Tech.* 11.11 (2018), pp. 5965–5979. DOI: 10.5194/amt-11-5965-2018. URL: https://www.atmos-meas-tech.net/11/5965/2018/ (cit. on p. 2).

[8] Alessandro Battaglia, Simone Tanelli, and Pavlos Kollias. «Polarization Diversity for Millimeter Spaceborne Doppler Radars: An Answer for Observing Deep Convection?» In: *J. Atmos. Ocean. Tech.* 30.12 (2013), pp. 2768–2787. DOI: 10.1175/JTECH-D-13-00085.1. eprint: https://doi.org/10.1175/JTECH-D-13-00085.1. URL: https://doi.org/10.1175/JTECH-D-13-00085.1 (cit. on p. 2).

[9] Alessandro Battaglia and Pavlos Kollias. «Error Analysis of a Conceptual Cloud Doppler Stereoradar with Polarization Diversity for Better Understanding Space Applications». In: *J. Atmos. Ocean. Tech.* 32.7 (2015), pp. 1298–1319. DOI: 10.1175/JTECH-D-14-00015.1. eprint: https://doi.org/10.1175/JTECH-D-14-00015.1. URL: https://doi.org/10.1175/JTECH-D-14-00015.1 (cit. on p. 2).

[10] A. Battaglia, A. Illingworth, and M. Wolde. «Wivern: a New Satellite Concept to Provide Global in-Cloud Winds, Precipitation and Cloud Properties». In: *IGARSS 2018 - 2018 IEEE International Geoscience and Remote Sensing Symposium*. 2018, pp. 901–902. DOI: 10.1109/IGARSS.2018.8517619 (cit. on p. 3).

[11] F. E. Scarsi, A. Battaglia, F. Tridon, P. Martire, R. Dhillon, and A. Illingworth. «Mispointing characterization and Doppler velocity correction for the conically scanning WIVERN Doppler radar». In: *Atm. Meas. Tech.* 17.2 (2024), pp. 499–514. DOI: 10.5194/amt-17-499-2024. URL: https://amt.copernicus.org/articles/17/499/2024/ (cit. on pp. 4, 7).

[12] David Burns, Pavlos Kollias, Aleksandra Tatarevic, Alessandro Battaglia, and Simone Tanelli. «The performance of the EarthCARE Cloud Profiling Radar in marine stratiform clouds». In: *J. Geophys. Res. Atm.* 121.24 (2016), pp. 14, 525–14, 537. DOI: 10.1002/2016JD025090. eprint: https://agupubs.onlinelibrary.wiley.com/doi/pdf/10.1002/2016JD025090. URL: https://agupubs.onlinelibrary.wiley.com/doi/abs/10.1002/2016JD025090 (cit. on p. 4).

[13] K. Lamer, P. Kollias, A. Battaglia, and S. Preval. «Mind-the-gap part I: Accurately locating warm marine boundary layer clouds and precipitation using spaceborne radars». In: *Atm. Meas. Tech. Disc.* 2020 (2020). accepted for publication in AMT, pp. 1–29. DOI: 10.5194/amt-2019-473. URL:

https://www.atmos-meas-tech-discuss.net/amt-2019-473/ (cit. on p. 4).

[14] A. Battaglia, M. Wolde, L. P. D'Adderio, C. Nguyen, F. Fois, A. Illingworth, and R. Midthassel. «Characterization of Surface Radar Cross Sections at W-Band at Moderate Incidence Angles». In: *IEEE Trans. Geosci. Remote Sens.* 55.7 (2017). 10.1109/TGRS.2017.2682423, pp. 3846–3859 (cit. on pp. 4, 47).

[15] William Henson, Ronald Stewart, and David Hudak. «Vertical reflectivity profiles of precipitation over Iqaluit, Nunavut during Autumn 2007». In: *Atmospheric Research* 99.2 (2011), pp. 217–229. ISSN: 0169-8095. DOI: https://doi.org/10.1016/j.atmosres.2010.10.009. URL: https://www.sciencedirect.com/science/article/pii/S0169809510002668 (cit. on p. 5).

[16] D Hudak, B Currie, R Stewart, P Rodriguez, J Burford, N Bussières, and B Kochtubajda. «Weather systems occurring over Fort Simpson, Northwest Territories, Canada, during three seasons of 1998–1999: 1. Cloud features». In: *Journal of Geophysical Research: Atmospheres* 109.D23 (2004). Citations: 9. DOI: 10.1029/2004JD004876. URL: https://doi.org/10.1029/2004JD004876 (cit. on p. 5).

[17] *Orographic Precipitation*. https://kbkb-wx.blogspot.com/2014/04/orographic-precipitation.html. Accessed: 2024-01-30 (cit. on p. 6).

[18] William A. Holm Mark A. Richards James A. Scheer. *Principles of Modern Radar*. SciTech Publishing, Inc.,https://citeseerx.ist.psu.edu/document?repid=rep1&type=pdf&doi=8da4c3b56c227db379e0d454a0285f84fba8ee1f (cit. on pp. 10, 11).

[19] Fawwaz T. Ulaby and M. Craig Dodson. *Handbook of Radar Scattering Statistics for Terrain*. Remote Sensing Library. Hardcover. Norwood, MA: Artech House, 1991 (cit. on p. 19).

[20] *nasa.gov*. https://www.earthdata.nasa.gov. Accessed: 2024-02-18 (cit. on p. 28).

[21] *Antenna Basics*. https://cdn.rohde-schwarz.com/pws/dl_downloads/ premiumdownloads/premium_dl_brochures_and_datasheets/ premium_dl_whitepaper/Antenna_Basics_8GE01_1e.pdf. Accessed: 2024-03-23 (cit. on p. 37).

[22] R. Meneghini and T. Kozu. *Spaceborne weather radar*. Artech House, 1990 (cit. on p. 47).

[23] F. T. Ulaby, R. K. Moore, and A. K. Fung. *Microwave Remote Sensing Active and Passive*. Artech House, Boston, 1986 (cit. on p. 47).

[24] A. Battaglia et al. «Spaceborne Cloud and Precipitation Radars: Status, Challenges, and Ways Forward». In: *Reviews of Geophysics* 58.3 (2020). e2019RG000686 10.1029/2019RG000686, e2019RG000686. DOI: 10.1029/2019RG000686. eprint: https://agupubs.onlinelibrary.wiley.com/doi/pdf/10.1029/2019RG000686. URL: https://agupubs.onlinelibrary.wiley.com/doi/abs/10.1029/2019RG000686 (cit. on p. 58).

[25] A. J. Illingworth et al. «The EarthCARE Satellite: The Next Step Forward in Global Measurements of Clouds, Aerosols, Precipitation, and Radiation». In: *Bull. Amer. Met. Soc.* 96.8 (2015), pp. 1311–1332. DOI: 10.1175/BAMS-D-12-00227.1. eprint: https://doi.org/10.1175/BAMS-D-12-00227.1. URL: https://doi.org/10.1175/BAMS-D-12-00227.1 (cit. on p. 63).